KINETICS BASED CHARACTERIZATION OF STRUVITE DISSOLUTION

BY

SAMUEL ENRIQUE AGUIAR

THESIS

Submitted in partial fulfillment of the requirements
for the degree of Master of Science in Environmental Engineering in Civil Engineering
in the Graduate College of the
University of Illinois at Urbana-Champaign, 2019

Urbana, Illinois

Adviser:

Assistant Professor Roland D. Cusick

ABSTRACT

As phosphorus removal and recovery has become the new standard of wastewater treatment new technologies have quickly been implemented to meet the task. The Ostara Pearl is a crystallizer technology well known in the field of struvite precipitation for plants equipped with enhanced biological phosphorus removal (EBPR). By feeding anaerobically digested EBPR sludge to the Pearl and dosing Mg, struvite precipitation is induced for high rates of P removal. However, one downfall of crystallizers is the generation of poorly characterized fine particulate matter during normal operation, which leave the reactor and disrupt EBPR efficacy. The main objective of this work was to characterize the dissolution of field grown struvite from an Ostara Pearl reactor. Dissolution rate constants between 0.94 and 2.61 mm/min were found for field grown struvite using the shrinking object model – a surface area dependent empirical kinetics-based dissolution model. Enhanced solubility of some field recovered struvite relative to reference struvite was also observed in short-term experiments leading to a need a deeper characterization of those samples. Long-term dissolution experiments, used to characterize the dissolution of any co-precipitants, found little Ca, Fe, and K content in field grown struvite. XRD and FTIR were used to identify any physical and chemical differences in field grown struvite samples which exhibited increased solubility compared to a reference struvite sample. Dittmarite ($MgNH_4PO_4*H_2O$) and another unknown crystalline solid were found to potentially lead to enhanced solubility. The importance of characterizing plant specific struvite was noted when instances of enhanced solubility were seen in samples which exhibit distinct FTIR bands when comparing surface to internal spectra.

ACKNOWLEDGEMENTS

I would like to thank my advisor Roland D. Cusick. In my time here you have always trusted in my work and ability. Our discussions were always fruitful and helped me broaden my vision of what the environmental engineering field is and should be. Thank you for your mentorship thus far and continued support as I enter my doctoral program.

I want to give thanks to Manying Zhang for her indispensable work in the lab. Your help turned what could have been reoccurring long nights on the 4th floor into manageable days that kept me motivated for the next. I hope a student of your caliber can help you in your own future graduate work.

I also want to thank our industry partner Ostara Nutrient Recovery Technologies Inc. for providing the solids samples tested here. I also thank Adrian Romero, Tom Johnson, Rachel Lee, Mikaela Verigin, and Leon Downing for their input during the course of this work.

Finally, I give thanks to the countless friends I have made throughout my time so far at UIUC. You have made Champaign more than an endless cornfield and a place to truly remember.

DEDICATION

I dedicate this work to my girlfriend Brianna Dahlquist. You have always believed in and supported me throughout my education. Thank you for coming to Champaign and your continued trust in our future together. I promise we will live somewhere warm in the future – you pick this time.

I also dedicate this work to my parents, Sam and Betty Aguiar, and my brother Danny Aguiar who even though were thousands of miles away felt like they were here with me throughout my degree.

R.I.P. Toby

TABLE OF CONTENTS

CHAPTER 1: INTRODUCTION

Managing phosphorus (P) within the Food-Energy-Water (FEW) network is essential for securing P fertilizers necessary for meeting projected food demands and preventing excess P leaching into waterways from agricultural runoff [1], [2] and municipal water resource recovery facilities (WRRF) effluent [3]. While sources of phosphate rock in the world are projected to grow and should easily meet the projected 45 Mt P 2020/2021 global fertilizer demand in the near term [4], uncertainties in future supply continue to exist due to 75% of the world's current P reserves being held by Morocco alone [5]. The emergence of eutrophication events related to excess nutrient runoff are well documented both in the U.S. [6]–[8] and around the world [9], [10]. In freshwater cases, P plays a key role in controlling eutrophication by promoting quick cycles of plant growth and decay [11] which favors the growth of simple organisms such as algae and phytoplankton over higher order macro-organisms [12]. The eventual decay of eutrophication induced algal blooms results in hypoxic conditions that disrupt established natural ecosystems.

To combat eutrophication, P recovery in the U.S. has been driven by state and national level regulation through the Clean Water Act (CWA) enforced by the U.S. EPA or authorized state bodies. The CWA requires all point source polluters that discharge into "a water of the U.S." to carry a National Pollutant Discharge Elimination System (NPDES) permit. This has led to an increased focus on the effluent of WRRFs across the country as clear point source polluters. Of the 4,420 "major" (1 ≥ MGD) water treatment plants in the U.S. in 2016, only 24% have any numeric P effluent limits through their NPDES permits [13]. However, by 2021, 26 states and 5 U.S. territories are expected to implement quantitative total N and total P water quality standards that are used to facilitate the NPDES permitting process [14].

Enhanced biological phosphorus removal (EBPR) has become the preeminent method of biological P removal used to meet the P effluent limits set in NPDES permits. EBPR processes rely on uptake of P by phosphorus-accumulating organisms (PAO) to reduce effluent P concentrations down to ~0.1-0.2 mg/L [15]. EBPR processes are composed of a two-stage anaerobic/aerobic chain followed by a clarifier during typical operation. In the anaerobic stage, P rich influent is mixed with activated sludge. In this stage, PAOs present in the activated sludge convert short chained carboxylic acids to polyhydroxyalkanoates while simultaneously hydrolyzing poly-P for energy [16]. Hydrolysis of poly-P results in the release of orthophosphate, further enriching the nutrient content of the wastewater. Following this stage, aerobic conditions allow for the growth of the PAOs and simultaneous uptake of orthophosphate to replenish poly-P hydrolyzed in the previous stage [16]. In the subsequent clarification stage, a P lean effluent is ready for additional treatments or discharge. The solids recovered are sent to the anaerobic stage to continue the EBPR cycle or are treated with anaerobic digestion, sludge thickening, or dewatering. In these cases, anaerobic conditions are possible leading to poly-P hydrolysis and conversion to orthophosphate by PAOs. Secondly, anaerobic digestion can lead to the production of ammonium as an end product of organic N (protein, urea) hydrolysis [17]. Once digestion has occurred and significant P and NH_4^+ are present in solution, precipitation of calcium phosphates and magnesium ammonium phosphates is possible even without addition of Ca and Mg [18].

To control the precipitation process and use it as a secondary method of P recovery, various precipitation reactors have been utilized as a sidestream process [19]–[21] treating supernatant resulting from EBPR sludge digestion and centrifugation. In recent history a large focus of P recovery at the WRRF has been on struvite ($MgNH_4PO_4*6H_2O$). Struvite crystallization has the potential to both reduce P recycling to mainline treatment and produce a P-rich fertilizer with the potential to reduce runoff. With the introduction of the Pearl rector in 2005, Ostara has become a leader in the P precipitation field with 22 installations worldwide since 2005 [22]. These reactors operate by dosing anaerobic digester supernatant rich with ammonium and orthophosphate from EBPR systems with magnesium in a pH-controlled environment to induce precipitation. The reactor is fed as an up-flow system and acts as a moving bed reactor. The catalyst particles in this reactor are large struvite “seeds” (4.5 mm - 350 μm) which provide thermodynamically favorable growth and nucleation sites for further struvite precipitation. As the seeds flow upwards through the reactor, the cross-sectional area of the rector increases in stages leading to three separate sedimentation zones. As particles increase in size due to crystal growth, they reside lower in the reactor where eventually they are collected at the bottom as Crystal Green [23] – a predominantly struvite based fertilizer.

One challenge faced by the widespread introduction of struvite recovery technologies such as the Ostara Pearl is the loss and dissolution of P rich fines in mainline treatment after washout from crystallizer reactors [24]. Historically, the dissolution of struvite has been largely ignored because of its low solubility ($pK_{sp} = 13.26$) [25] and a predominate focus on formation for recovery. However, recent reports of low crystallization yield and disruption of EBPR have elucidated the importance of monitoring fines production and loss [24], [26]. While P removal is typically satisfactory (~80%), yield as crystal green in Ostara Pearl reactors can sometimes drop to as low as 20% of the total influent P [24]. Models used for struvite crystallization, described in this work later, do not account for the generation of fines. Without this critical element of the well-documented phenomena, accurate optimization of these reactors is not possible when the impact of fines loss and dissolution is not considered.

A recent sensitivity analysis of an EBPR plant-wide model showed dissolution rate was a dominant factor in determining plant effluent P, especially in cases of low solids retention in the crystallization reactor [27]. However, this study did not account for particle size or surface area to determine dissolution rate. Instead, it relied on a simplified version of the general precipitation framework developed by Mbamba et al. [28] that only considers the degree of supersaturation in solution and total crystal mass in the system.

A lack of agreement exists in the literature on the base assumptions necessary to correctly model dissolution. Since the introduction of a strictly thermodynamics based model [29] for precipitation, many studies have built upon this framework for use in plantwide modelling [28], [30]–[32]. However, these studies simply assume precipitation and dissolution occur through the same mechanisms yielding no difference in dissolution/precipitation rate constants at equal super/under-saturations often disregarding particle size and surface area. For large particles that will easily settle in clarifiers, dissolution will not likely lead to significant changes in the concentration of inorganic P. However, for fines washed out from a crystallizer in the colloidal range (< 1 µm), the surface area to volume ratio is much higher and can lead to quick dissolution. One dissolution model which shows the link between dissolution and surface area is the Shrinking Object (SO) model [33]. The SO model was derived using classical chemical kinetics assumptions that focus on observations rather than assumed mechanisms. In this study, the SO model is used rather than a thermodynamics-based approach to determine the dissolution rate of field grown struvite to account for deviations from pure struvite dissolution.

Despite the availability of this model and other commonly accepted dissolution models, limited data is available on the dissolution rate constant, k, of struvite. Understanding struvite dissolution kinetics will allow kinetics-based plantwide models to more accurately predict the impact of fines loss on overall plant performance. The purpose then of this study is to fully characterize the dissolution rate of field recovered struvite for future modelling and WRRF design. In this investigation, there are three main objectives: 1) Determine the dissolution rate of field grown struvite, pure struvite, and pure hydroxyapatite at WWRF relevant temperatures; 2) Confirm the influence of particle size on dissolution rate predicted by the SO model by fitting time-series dissolution data to the linearized shrinking object model, and 3) Elucidate differences between dissolution behavior of various solids (field grown vs pure reference) tested.

CHAPTER 2: LITERATURE REVIEW

2.1 Why Recover Phosphorus?

In the U.S. and Europe, P recovery is increasingly becoming a requirement at the WRRF [34], [35]. In a traditional wastewater treatment plant design with activated sludge up to 30% P removal occurs naturally as biomass grows and is wasted as sludge [35]. This however is not likely to even reach the most lenient European standard of 2 mg/L for typical wastewater streams which can be as dilute as 10 mg P/L [36]–[39] or if treating industrial and agricultural waste concentrations in the hundreds of mg/L P are common [40], [41]. Two common methods exist for the removal of P from wastewater: 1) biological P removal [36] and 2) chemical P removal [42]. Biological P removal relies on the uptake of P as part of the regular metabolic activity of biomass. The P rich sludge formed can then be wasted or treated further. Chemical P removal is based on either iron or alum dosing. Both types of chemical P removal proceed through forming a metal-phosphate precipitant and then incorporate into larger metal hydroxide flocs. A chemical sludge is formed that can be separated and wasted. In most cases a combination of both is used to reach effluent P < 0.5 mg P/L [43]–[46].

2.2 New P removal and Recovery Strategies

As limits on WRRF effluent P concentration become more stringent (2 mg/L or below) [34], new technologies are emerging to enhance or replace the common P removal already in place with new goals of recovery rather than removal.

2.2.1 Ostara Pearl

The Ostara Pearl reactor is a continuous struvite crystallizer operated as an upflow moving bed reactor. The Pearl is specifically designed to remove P as a solid from highly concentrated (in terms of P and N) anaerobic digester centrate resulting from the digestion of EBPR sludge. By dosing the influent with magnesium and base (NaOH), struvite is supersaturated and precipitation is induced. The Pearl is initially seeded with struvite seed particles with diameters ~1 mm to allow for crystal growth and limiting primary nucleation. The reactor is shaped in a three-tier fashion with increasing cross-sectional area along the height of the reactor. This three-tier design allows for three flow regimes to develop and allows for collection of the largest particles at the bottom, suspension of growing particles in the middle section, and ideally retention of fines at the top [47], [48]. The resulting struvite product is marketed as a slow-release fertilizer named Crystal Green [23].

The first Pearl went into operation in 2009 at the Durham Advanced Wastewater Treatment Plant in Tigard, Oregon [48]. This reactor boasted 75% P recovery as struvite that was then sold as fertilizer, reduced alum costs related to previous chemical P removal, and reduced alum sludge handling. However, upsets do occur and the generation of fines in Pearl reactors has been reported. At the Nansemond Wastewater Treatment Plant between 10% and 85% TP removal was reported over the course of 9 months with low TP removal attributed to fines loss during what was considered the startup phase [47]. Another case of high removal (70-80% PO_4-P) was shown at the F. Wayne Hill Water Resource Center, but fines loss was initially reported leading to lower fertilizer production than expected for the amount of P removed [49]. As recently as 2015, the Madison Metropolitan Sewerage District reported ~30% TP removal during normal operation but saw an upset after operational modifications and dosing of ferric chloride in a thickening unit. During the upset feed and effluent TP were nearly identical (~ 0% TP removal) with a low fraction of soluble P indicating a huge loss of fine particles [50].

Efforts to reduce the fines loss seen at the Madison plant were recently demonstrated and focused on reducing the size of the seed particles used and reducing the size of harvested product [24]. By reducing the size of the seeds, more surface area per mass loading is present. Yields were increased from ~30% to ~70% TP removal. While promising, for plants as large as Madison (42 MGD), ~30% TP recycling is not ideal as it likely will lead to an increased need for VFA dosing and an increase in sludge production. To fully elucidate the implications fines may have on the future of crystallizers like the Ostara Pearl and the impact they have on overall plant performance, a thorough understanding of the thermodynamic driving force behind crystallization and its associated physical phenomenon is necessary.

2.2.2 WASSTRIP

The Waste Activated Sludge Stripping To Remove Internal Phosphorus (WASSTRIP) process was developed at by Clean Water Services to reduce the likelihood of nuisance struvite precipitation in anaerobic digesters fed with EBPR sludge *[48]* and to increase P mass diversion to struvite crystallizers. In pilot studies, WASSTRIP operated as a VFA dosing tank for EBPR sludge that would jump start the release of ortho P by PAOs *[51]*. Since no digestion occurs in WASSTRIP the resulting centrate is low in ammonia and does not cause precipitation of struvite. This supernatant can then be directly sent to a struvite crystallizer to remove as crystal green rather than as part of the anaerobic digester sludge. Plantwide modelling studies have been recently reported for integration of WASSTRIP at plants with the Ostara Pearl to understand the downstream benefits of the technology and optimization *[52], [53]*. A 2016 study found a pre-thickening procedure led to increased VFA production and ultimately more P release. Similar to the Ostara Pearl, a limited understanding of the technology at hand, hurried along by the need to remove P more efficiently has led to a need for modeling to fully grasp the plantwide benefits of the technology.

2.2.3 AirPrex

Another competing struvite precipitation technology is AirPrex by CNP [54]. Unlike the technologies discussed earlier, AirPrex increases solution pH by stripping CO_2 from digestate with air rather than adding base. Magnesium is dosed to promote struvite formation. This reactor is designed to operate between a digester and a sludge treatment technology (dewatering, thickening, etc.) such that the resulting struvite and organics rich slurry requires washing with a sand washer to be of product quality [55]. At the Metro Wastewater Reclamation District in Denver, Colorado, pilot studies [56] of an AirPrex reactor showed a reduction in dewatering polymer by up to 20% and up to 10% less solids hauling as a benefit of the technology. Similar to other crystallizer technologies discussed conversion of orthophosphate was high with up to 90% conversion, but the production of fines and entrapment of crystals within the biosolids lead to only 20% P recovery. The pilot study suggested the remaining balance of converted P remained in the biosolids but increases in reactor effluent TP indicate the production of fines that were not well characterized. The inclusion of a high organics loading in the streams fed to AirPrex increases the complexity of crystallization as favorable nucleation sites are ubiquitous. This technology again emphasizes the need to understand crystallization processes to fully optimize design.

2.3 Solubility: A Thermodynamics Perspective

Precipitation reactors are driven by a difference in the energy state of free ions in solution and their respective counterparts as a solid. The simplest measure of how far or close a solution is to equilibrium is saturation. Saturation is a measure of the ionic content of a solution and is related to the commonly known term solubility. A derivation of saturation for a general dissolution reaction is given here. First, we define a general dissolution reaction,

$$MX \leftrightarrow M^{+} + X^{-} \tag{1}$$

Solubility is defined by the free energy change observed during the dissolution of a solid at standard solution conditions and expressed as an equilibrium constant. This constant known as the solubility product, K_{sp}, follows the Arrhenius form shown in equation (2) with a unity prefactor.

$$K_{sp} = \exp\left(\frac{-\Delta G^{\circ}}{RT}\right) \tag{2}$$

In real systems, most solutions are not at equilibrium. Instead they are defined by the ionic activity product (IAP), a measure of how many ions are dissolved in solution. The IAP is mineral specific, such that separate IAP's must be calculated for each mineral that may potentially form.

$$IAP = \{M^{+}\}\{X^{-}\} \tag{3}$$

Determining whether a solution is in a state where precipitation is thermodynamically favorable relies on the difference between the magnitudes of the IAP and K_{sp}. Three cases are possible 1) undersaturation (IAP < K_{sp}), 2) equilibrium (IAP = K_{sp}), and 3) supersaturation (IAP > K_{sp}). A common definition used to compare the degree of saturation between different solutions or minerals is the saturation index (SI).

$$SI = \log\left(\frac{IAP}{K_{sp}}\right)^{1/z} \tag{4}$$

Here z indicates the number of component ions in the mineral in question. A solution is supersaturated when SI > 1, at equilibrium when SI = 0, and undersaturated when SI < 0. This definition is most useful to compare different minerals when $z_1 \neq z_2$.

Supersaturation of a solution is necessary but insufficient to determine if precipitation will occur within relevant time scales in a system. Crystal nucleation and growth kinetics both have dependence on SI (as C_{sat}) detailed further in sections 2.7 and 2.99. Given the dependence on SI, P recovery technologies relying on precipitation must have foresight into the potential minerals to be recovered as well as their respective K_{sp}.

2.4 Minerals Relevant to P Recovery

P recovery through precipitation has long relied on a small set of minerals which can generally be categorized either as magnesium ammonium phosphates (MAP), calcium phosphates (CaP), or other phosphate containing minerals (MP). Various minerals may be oversaturated in a single waste stream, but typically will fit the profile of a MAP, CaP, or MP rich stream dependent on the cations present. In most systems a salt with the preferred metal ion is added to ensure the correct product is recovered. Though CaP and MP have gained interest recently in P recovery literature, most research is on MAP recovery.

Struvite ($MgNH_4PO_4 \cdot 6H_2O$), k-struvite ($KMgPO_4 \cdot 6H_2O$) dittmarite ($MgNH_4PO_4 \cdot 8H_2O$), newberyite ($Mg(PO_3OH) \cdot 3H_2O$), and the trimagnesium phosphates bobierrite ($Mg_3(PO_4)_2 \cdot 8H_2O$) and cattitte ($Mg_3(PO_4)_2 \cdot 22H_2O$) have all been observed in solutions containing sufficient magnesium, ammonium, and phosphate ions [57], [58]. However, within the pH range of most waste streams (6-9), trimagnesium phosphates have never been noted to precipitate [59]. Similarly, precipitation of newberyite occurs below pH 6 and would not be relevant to P recovery [30]. Struvite which has been documented between neutral to high pH [58] and its potassium isomorph are the only relevant MAPs.

Unlike MAP, which forms a succinct set of minerals at wastewater relevant conditions, calcium phosphates (CaP) include a larger family of potentially formed phases. These phases include amorphous calcium phosphate (ACP – $Ca_3(PO_4)_2$), dicalcium phosphate dihydrate (DCPD – $CaHPO_4 \cdot 2H_2O$), octacalcium phosphate (OCP - $Ca_8H_2(PO_4)_6 \cdot 5H_2O$), and hydroxyapatite (HAP - $Ca_{10}(PO_4)_6(OH)_2$). In most wastewaters including those with substantial Mg^{2+}, HAP is the most thermodynamically stable phase due to its low solubility. However, spontaneous growth of HAP without a precursor phase has not been shown outside of organic frameworks with pore sizes small enough to promote direct HAP growth [60]. This is due to the complex crystal structure of hydroxyapatite yielding large nucleation barriers and corresponding sluggish nucleation kinetics compared to simpler phases such as ACP, the generally accepted master precursor phase to all other calcium phosphates including OCP, DCPD, and HAP [61].

Though there is much disagreement on the true unit cell of ACP [62]–[64], what is clear is that prenucleation clusters (PNC), which are loosely ordered complexes of calcium and phosphate ions, go through some degree of transformation from free ions to the higher ordered aggregates known as ACP. ACP growth is distinct from other crystals mentioned here including struvite, in that classical nucleation theory does not accurately explain the growth mechanisms which have been observed. ACP formation is most accurately represented as an aggregation process where discrete ions form PNC's which then go on to form larger polymer-like networks [63]. When densified further the phase is typically recognized as ACP. Though it is weakly characterized and even less understood from a perspective of formation mechanisms, ACP precipitation is a requirement of most systems where HAP is a desired end product.

Finally, an emerging area of phosphorus recovery is by precipitation of aluminum and iron salts, which have long been known for their coagulative properties and cost effectiveness in the case of iron [65], [66]. Iron phosphates are also attractive from a reuse perspective as P is efficiently mobilized by natural processes in sediments and soils [42]. In WWTP, iron phosphates form either as iron phosphate minerals or adsorption complexes which involve adsorption of orthophosphates on iron oxides [67]–[69]. The phosphorus recovery relevant phases studied in literature are $Fe_3(PO_4)_2$ and the iron oxides am-FeOOH and other hydrous ferric oxides for their P adsorbing properties [42], [67], [69], [70]. Though $FePO_4$ has been studied, it was shown to not precipitate below pH 5 and therefore not relevant to wastewater systems [69]. More complex and less soluble iron phosphates have also been studied including $Fe_{2.5}P0_4(OH)_{4.5}$, $Fe_{1.6}H_2P0_4(OH)_{3.8}$, and $Fe_3(P0_4)_2.8H_2O$, though based on fitting experiments with real wastewaters [68], [70]. Because of the known adsorption of phosphorus on iron oxides, these studies cannot be used as definitive proof of an insoluble iron phosphate. However, they do point towards P adsorption as a significant removal mechanism.

2.5 Solubility Product K_{sp}

The solubility of potential P recovery phases varies widely, but at pH ranges relevant to wastewater treatment HAP is the dominant and most thermodynamically stable phase. Table 2 gives K_{sp} values for relevant solids phases at 25 °C.

Table 1. K_{sp} of Relevant Phosphorus Containing Minerals

Phase	**Formula**	**pK_{sp} (25 °C)**	**M:P$^{\alpha}$**	**Reference**
Struvite	$MgNH_4PO_4{\cdot}6H_2O$	13.26	1	[25]
k-struvite	$KMgPO_4{\cdot}6H_2O$	12.2	2	[71]
Dittmarite	$MgNH_4PO_4{\cdot}6H_2O$	13.34	1	[72]
DCPD	$CaHPO_4{\cdot}2H_2O$	6.59	1	[61]
OCP	$Ca_8H_2(PO_4)_6{\cdot}5H_2O$	49.6^{β}	1.33	[73]
ACP	$Ca_3(PO4)_2^{*}$	25.7	1.5	[61]
HAP	$Ca_{10}(PO_4)_2(OH)_2$	58.65^{β}	1.67	[74]
Iron Phosphate	$Fe_3(PO_4)_2$	36	1.5	[69]

*Assumed formula, $^{\alpha}$Metal to Phosphorus ratio, $^{\beta}$pKsp values for half unit cell

2.6 Modelling Crystal Growth, the Population Balance, and Crystallization Phenomena

The use of crystallization has long been a part of human culture [75] and is now a staple unit op in industrial processes [76], [77]. Records exist of a Chinese print from 2700 B.C. which detailed controlled and intended crystallization through evaporation to create salt [75]. As crystallization technologies have progressed and become a corner stone of the pharmaceutical and biotechnology industry [78], there has been an expressed need to accurately model crystallization at scale.

In modelling crystallization technologies, constructing a valid governing equation requires the incorporation of all the major phenomenon observed in the birth and death of a crystal. One of the most common types of continuous crystallization reactors is the mixed-suspension mixed-product-removal (MSMPR) crystallizer [79]. In this type of crystallizer an influent with a known flow rate, solution chemistry, and count of crystals is fed continuously to a main reactor. In the MSMPR reactor, CSTR equivalent assumptions are made with regards to perfect mixing and the resulting uniformity in particle size distribution between the crystals in the effluent and in the main tank. For simplification of the MSMPR case it is assumed breaking of crystal is negligible, but it is noted that attrition, the creating of nucleus sized particles from physical collisions, does occur. It is also assumed that crystals produced in the MSMPR will follow a regular crystal habit, therefore a single dimensional length characteristic, L, can be used to describe the size of the crystal and shape factors can be used to calculate other extensive properties such as mass or surface area.

To generate a set of governing equations for the MSMPR reactor three major processes must be considered: 1) nucleation, 2) crystal growth/dissolution, and 3) aggregation. In all cases of crystallization, a thermodynamic driving force leads to supersaturation within the liquid phase.

This supersaturation drives nucleation leading to newly formed particles in the nanometer scale either homogenously in solution or heterogeneously on thermodynamically favorable nucleation sites on solid impurities suspended in solution. At the same time this supersaturation drives further crystal growth once nucleates are formed. Finally, if sufficient mixing occurs or if the difference in particle sizes allows for collision during sedimentation, it is possible that particles form larger aggregates.

For reactor design and process engineering, it is of use to have a governing equation which relates all three processes to the particle size distribution of the crystals in the MSMPR as a function of time. This governing equation, known as the population balance equation (PBE), was developed for MSMPRs with the assumptions described above with size independent growth and constant reactor volume by [80]:

$$\frac{\partial n}{dt} + G\frac{\partial n}{\partial L} + (D - B) = -\sum_{k} \frac{n_k Q_k}{V} \tag{5}$$

Here, n is the population density, G is growth rate, (D-B) is the difference between the death and birth rates of crystals, n_k the population density in stream k, Q_k the flow of stream k, and V the volume of the MSMPR reactor. The death and birth functions work to describe the sudden appearance or disappearance of a particle of a certain size class (i.e. breakage of a particle leading to death of that particle but birth of two smaller sized particles). The term on the right-hand side of the equation relates to crystals in the reactor inlet and outlets.

The PBE derived by [80] does not explicitly relate nucleation rates and aggregation with other terms in the equation, but other prior works have shown discrete systems where expressions for aggregation rates and nucleation rates can appropriately replace the (D-B) term [31], [81]. The PBE used in conjunction with a mass balance equation and assumptions on the thermodynamic driving forces has been previously used to model struvite precipitation reactors and estimate nucleation rate [31], [32], [82], growth rate [31], [32], [82], and aggregation rates [31], [32]. Though the crystallization reactors in struvite precipitation technologies today are more complex with various degrees of saturation and flow regimes throughout the length of the reactor, the physical processes which govern struvite crystallizers are the same.

Other models also exist and are very common in the struvite precipitation modelling literature but miss the fundamental nature particle size plays in precipitation technologies and the importance of the particle size distribution when designing crystallizers. Due to the difficulties in accurately measuring particle size in real time and at the size range necessary to fully characterize crystallization (nano- to millimeter diameter), simplified models have been routinely employed. These types of models are described as kinetics-based [28], [30], [83]–[86] models and typically rely on measuring the disappearance of a solid phase constituent ion (i.e. Mg, P, N) and fitting to assumed rate equations to determine rate constants. Regardless of whether a kinetics-based model is used or the PBE is employed, it is necessary to assume expressions for nucleation rate, crystal growth rate, and aggregation rate for later fitting. These parameters all have a well-developed theoretical basis described further here.

2.7 Nucleation

In systems like wastewater where coprecipitation of struvite, CaP, and other minerals is thermodynamically favorable, the kinetics of crystal nucleation is relevant in determining if crystals will form within the timescales in question. Though crystallization can occur homogenously or heterogeneously, the abundance of solid-liquid interfaces in wastewater treatment systems means most nucleation occurs heterogeneously. However, theory on homogenous nucleation can apply to heterogenous nucleation given that the surface is similar to the forming nuclei in terms of lattice structure [87].

2.7.1 Classical Nucleation Theory

Classical nucleation theory (CNT) is a based on the minimization of free energy of ions in solution by precipitation. The change in free energy of a spherical nucleus can be described as a two-component system as shown in equation 6: a bulk term describing the homogenous formation of a solid from free ions and a surface term describing the newly formed surface during precipitation [88].

$$\Delta G_n = \frac{-4\pi r\hat{}3}{3V_m} KT \ln(S) + 4\pi r\hat{}2\gamma \tag{6}$$

Here r is the radius of the forming nuclei, $V_m$the molecular volume, K the Boltzmann constant, T the temperature of the fluid, S the supersaturation ratio, and γ the net surface energy of the solid-liquid interface. When first forming, the molecules on the surface of the nuclei are not bonded and have excess energy resulting in a larger surface energy term than the bulk term. As more molecules bond with the nuclei the radius of the particle increases eventually leading to a negative free energy change. Physically, a larger fraction of the molecules are within the bulk than on the surface of the particle and the bulk term becomes larger than the surface energy term.

This implies an energy barrier exists at a critical radius (r*) calculated by differentiating equation 6 with respect to r.

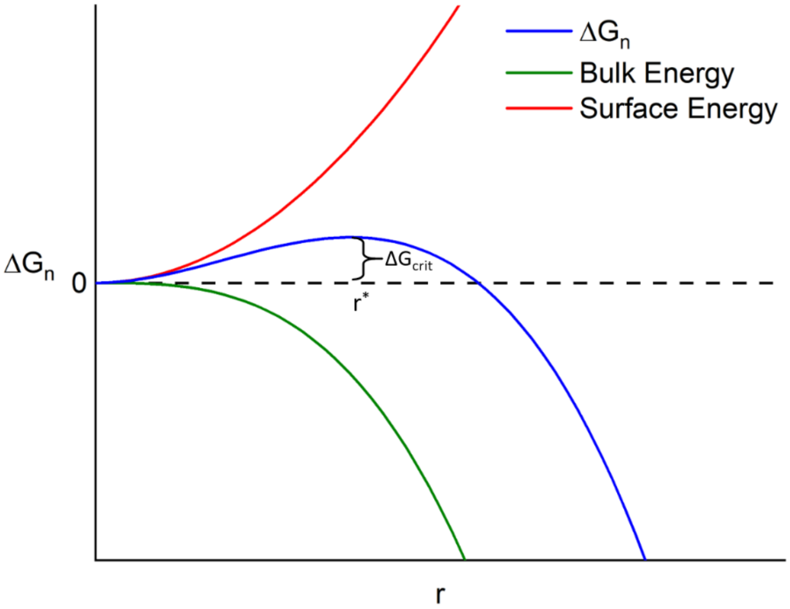

Figure 1. Free energy change of nucleation

$$r^* = \frac{2\gamma}{KTln(S)} \tag{7}$$

This can be used to calculate the magnitude of the energy barrier to nucleation shown in equation 8.

$$\Delta G_{crit} = \frac{16\pi\gamma^3 V_m^2}{3K^2T^2 \ln(S)^2} \tag{8}$$

Nucleation rate, J, is then defined using the Arrhenius form,

$$J = A \exp\left(\frac{-\Delta G_{crit}}{KT}\right) = A \exp\left(\frac{-16\pi\gamma^3 V_m^2}{3K^3T^3\, ln(S)^2}\right) \tag{9}$$

Where A is an empirical prefactor. Under the assumption that classical nucleation theory holds for a system, maximization of nucleation rate would be achieved by decreasing the net surface energy term and increasing the supersaturation ratio. Practically, this means the materials used for seeding crystallization reactors play an important role in determining reactor kinetics. In the calcite system, template directed nucleation has experimentally shown rate dependence on γ[89].

The interfacial free energy is composed of three interfacial interactions [89], [90] shown in equation 10.

$$\gamma = \gamma_{CL} - h(\gamma_{SL} - \gamma_{CS}) \tag{10}$$

Where γ_{CL} denotes crystal-liquid interfacial free energy, γ_{SL} the substrate-liquid interfacial free energy, and γ_{CS} is the crystal-substrate interfacial free energy. The h parameter describes a nucleus shape factor related to interface surface area ratios. In the calcite system which follows CNT, the effect of varying surface chemistry, thereby changing γ through γ_{CS}, has shown good agreement with equation 9 and was correlated to the free energy of binding ΔG_b [90] shown in equation 11.

$$\Delta G_b = a(\gamma_{CL} - \gamma_{SL}) - a\gamma_{CS} \tag{11}$$

In equation 11, a is the contact area between the crystal and substrate. This study implies that for systems where CNT applies, estimations of nucleation rate can be made with limited molecular information (V_m), solution supersaturation (S), and interfacial free energies.

Further research into the surface chemistry dependence of γ showed that differing charge density by varying the surface used (in a physical sense altering γ_{SL}) was the controlling factor on the barrier to nucleation followed by lesser dominance of γ_{CS} which was related to slight differences in surface structure rather than surface chemistry [89].

A majority of the studies on characterizing the crystallization of struvite have focused on estimating nucleation rate through induction time, t_{ind}, or particle counts. Induction time is simply defined as the inverse of nucleation rate. If induction time is linearized using a log transform this becomes,

$$\log(t_{ind}) = \frac{A}{\log(S)} + B \tag{12}$$

Where $A = \frac{-16\pi\gamma^3 V_m^2}{3K^3T^3}$ and $B = \log(A)$, the definition of B recalls the prefactor A from equation 9.

2.7.2 Nonclassical Nucleation Theory

In contrast to CNT, nonclassical nucleation pathways do not directly form the final thermodynamically stable phase but form intermediate prenucleation clusters which can then aggregate to form the final phase or if larger than the critical radius, exhibit molecular growth. Secondly, these clusters form without the need for solution supersaturation, a prerequisite to nuclei formation under classical nucleation theory [91]. The formation of intermediate prenucleation clusters has been shown experimentally for calcium phosphate precipitation [63], [92] with the initial formation of amorphous calcium phosphate clusters in solution, followed by template directed densification of these clusters, and eventual transition to crystalline hydroxyapatite.

One proposed nonclassical nucleation theory derived from computational studies is the two-step mechanism. Though originally used to study molecules with shortrange interactions such as proteins, density functional theory calculations showed that for atomic fluids which follow lennard-jones interactions, a general mechanism of the formation of a disordered phase followed by crystallization gives a pathway with local minima corresponding to a metastable intermediate phase with lower activation energies than what is expected from CNT [93]. In many cases, the two step mechanism arises through the solvents ability to promote or hinder intermolecular hydrogen bonding which can also lead to variance in the structure of the final solid [94], [95].

2.8 Aggregation

Aggregation processes are a result of electromagnetic interactions between small particles dispersed in solution. At the colloidal particle size scale (10^{-9} m to 10^{-6} m), gravitational forces and hydrodynamic effects are negligible until particles have aggregated to sizes which undergo observable sedimentation ($< 10^{-6}$ m) [96]. Historically, DLVO theory has been the primary method of understanding colloidal stability as it includes both repulsive and attractive forces through the combination of electrical double layer theory and the Van der Waals forces.

2.8.1 Pair Potentials and Intermolecular Forces

At the intermolecular scale, interactions between molecules can be simplified to pair potentials that depend on molecular properties such as hard sphere diameter, charge, dipole moment, and polarizability. Pair potentials can be generalized to the form shown in equation 13.

$$w(r) = \frac{-c}{r^n} \tag{13}$$

Where w(r) is the pair potential between two molecules at a distance r, c is a constant indicating the magnitude of the pair potential, and n indicates the scale over which the interaction is relevant. When n > 3, the interactions can be considered short range. In common use today are variations on the semi-empirical Mie potential which accounts for both attractive and repulsive interactions at various scales [97].

$$w(r) = \frac{-A}{r^n} + \frac{B}{r^m} \tag{14}$$

Most notably the Lennard-Jones model has been used to determine pair potentials between noble gases and uncharged particles [98].

$$w(r) = \frac{-A}{r^6} + \frac{B}{r^{12}} \tag{15}$$

Pair potential is related to the force between the two particles as given in equation 16.

$$F(r) = -\frac{dw(r)}{dr} \tag{16}$$

Given this relationship, general derivation schemes of pair potentials include first defining the force between the two particles followed by integration to reach w(r). Summation of the forces felt by all the molecules in a system gives rise to forces felt by surfaces as shown in the work of Hamaker [99]. Many types of interactions are possible with varying strength, but one the strongest interactions come from charge-charge interactions. These interactions become most relevant when considering the interface between a solid and a liquid due to charge separation. Another class of interactions falls under Van der Waals forces. These forces are related to dipole-dipole, dipole-non-polar, and non-polar-non-polar interactions.

2.8.2 Surface Charge in Aqueous Environments

When in solution, surfaces undergo charge separation due to 1) differences in ion affinity, 2) surface ionization, 3) physical constraint of charge in a phase, and 4) isomorphous substitution [100], [101]. These effects contribute to the creation of a diffuse ion gradient surrounding a charged particle surface [101].

In the case of low potential difference between the particle surface and the diffuse layer, large particle size compared to the diffuse layer thickness, and symmetrical electrolytes, a combination of the one-dimensional form of the Poisson equation (equation (17) and the Boltzmann distribution (equation 18) through charge density ρ relates potential to distance normal to the particle surface (equation 19).

$$\frac{d^2\Psi}{dx^2} = -\frac{\rho}{\varepsilon\varepsilon_0} \tag{17}$$

$$\frac{n_i}{n_{i0}} = \exp\left(\frac{-z_i e\Psi}{kT}\right) \tag{18}$$

$$\Psi = \Psi_0 \exp(-\kappa x) \tag{19}$$

In these equations, Ψ is potential, x is the distance from the particle surface, ε_0 is the permittivity in vacuum, ε is the relative permittivity of the medium, n_i is the concentration of ith-type ions, n_{i0} is the concentration of ith-type ions at an infinite distance from the surface, z_i is the valence of the ith-type ion, e is the charge of an electron, k is the Boltzmann constant, T is the temperature of the medium, Ψ_0 is the potential at the surface of the particle, and κ is the inverse of the double layer thickness.

For cases where low potentials are not a good assumption, Guoy-Chapman theory provides a result similar in form to that of equation 19 [101], [102]. Similar results shown in equation 20 have also been found for particles which do not meet the requirement of a large size relative to the diffuse layer thickness and are derived for spherical geometry [103].

$$\Psi = \Psi_0 \left(\frac{R_S}{r}\right) \exp(-\kappa(r - R_s)) \tag{20}$$

Where R_s is the radius of the particle and r is the distance away from the center of the particle.

2.8.3 Electrical Double Layer Repulsion

Now that an expression for the potential normal to a charged surface has been derived, a corresponding force equation can be found using equation 21. It was shown that for two flat plates at a distance l the area normalized repulsion force is as follows [103],

$$F(l) \cong 64 n_0 k T \gamma_0^2 \exp(-l\kappa) \tag{21}$$

Where γ_0, an expression derived in Guoy-Chapman theory [101], is defined in terms of surface potential as,

$$\gamma_0 = \frac{\exp\left(\frac{ze\Psi_0}{2kT}\right) - 1}{\exp\left(\frac{ze\Psi_0}{2kT}\right) + 1} \tag{22}$$

Equation 22 shows that for any separation distance when $\gamma_0 > 0$, the force felt by the plates is positive and therefore repulsive.

Due to custom, the interaction energy rather than force is plotted against separation distance and is given as,

$$w(l) = \frac{64 n_0 k T \gamma_0^2}{\kappa} \exp(-l\kappa) \tag{23}$$

In this work, this equation will be integrated with other attractive interaction energy terms later to determine overall interaction behaviors. However, this solution scheme is applicable to all geometries not just flat plate approximations. Generally, the Poisson-Boltzmann equation is solved for potential in terms of a characteristic length and then combined with other interaction energies to determine overall interaction behaviors.

2.8.4 Van der Waals Attraction

Though electrical double layer theory explains repulsions well, a limited understanding on the origins of attractive intermolecular forces was a long-standing hindrance in the field of colloidal stability [102]. One of the first successful attempts at explaining the attractive forces observed was through Van der Waals (VDW) Forces. The VDW forces arises from three separate intermolecular interactions namely dipole –dipole, dipole – non-polar, and non-polar – non-polar interactions. Differing from charge-charge interactions seen in electrical double layer repulsion, these interactions originate from existing permanent or induced dipoles, in the case of non-polar molecules, and depend on the molecules dipole moment (u), polarizability (α), first ionization potentials (I). These interactions are also known as Keesom energy, Debye energy, and London dispersion energy respectively. The pair potentials for each of these terms is given in table 2.

Table 2. Van der Waals interaction energies [99]

	Interaction Type	Interaction Energy w(r)
Keesom energy	Dipole – dipole	$\frac{-u_1^2u_2^2}{3(4\pi\varepsilon\varepsilon_0)^2kT}*\frac{1}{r^6}$
Debye energy	Dipole – non-polar	$\frac{-u^2\alpha}{(4\pi\varepsilon\varepsilon_0)^2}*\frac{1}{r^6}$
London dispersion energy	Non-polar — non-polar	$-\frac{3}{4}\frac{I\alpha^2}{(4\pi\varepsilon\varepsilon_0)^2}*\frac{1}{r^6}$

The magnitude of each of the components to VDW forces is strongly dependent on the type of molecules interacting. London dispersion energies will always be present, but both Debye energy and Keesom energy depend on the existence of at least one permanent dipole in the system. Often, London dispersion energy is the largest interaction type, but this can fail when very strong dipole moments are observed such as in water [103].

Hamaker generalized the VDW interaction expressions for surfaces rather than intermolecular interactions for a variety of geometries including flat plates and spheres and introduced the Hamaker constant, A [99]. This constant is defined as shown in equation 24.

$$A = \pi^2 C\rho^2 \tag{24}$$

Where C is the coefficients seen in each of the VDW interaction energy components. For a flat plate, Hamaker found the interaction energy to be defined as shown in equation 25.

$$w(l) = \frac{-A}{12\pi l^2} \tag{25}$$

This interaction energy is negative for all separation distances (l) and indicates an attractive force between the two plates. This equation can then be combined with equation 24 to provide an overall interaction energy used in DLVO theory.

2.8.5 DLVO Theory

Irreversible aggregation takes place when attractive Van der Waals forces are greater than repulsion originating from the electrical double layer. DLVO theory attempts to account for these two interactions by assuming an additive nature applies to the two interaction energies as shown in equation 26.

$$w_{tot}(r) = w_{VDW} + w_{EDR} = \frac{-A}{12\pi l^2} + \frac{64 n_0 k T \gamma_0^2}{\kappa} \exp(-l\kappa) \tag{26}$$

Several cases can arise from this type of analysis, but most feature a primary minimum, a secondary minimum, and an energy barrier. The secondary minimum is a separation distance at which particles will aggregate but can be reversibly separated. If the particles collide with enough kinetic energy, the energy barrier to aggregation is overcome and the particles can enter the primary minimum separation distance in a non-reversible process. Though inclusion of only VDW and electrical double layer repulsion indicates that as $r \rightarrow 0$ then $w(r) \rightarrow -\infty$, this does not correspond to a physically realizable attraction. Inclusion of other non-DLVO terms into the net interaction energy equation can give more realistic results indicating repulsion at very small separation distances. More information on those repulsive interactions are given in other texts [101], [103].

2.8.6 Modelling Aggregation

Although DLVO theory shows a clear physical motivation for the attraction and repulsion of small colloidal particles at short distances, it does not account for aggregation of particles dispersed in a medium at distances where DLVO forces would be negligible. In fact, DLVO forces only occur at such small scales, it is often assumed collisions between particles are independent of them [104]. Modelling of aggregation processes therefore relies on various transport rates to describe particle collisions.

The Smoluchowski approach [104], [105] assumes particles are initially the same size and spherical, but after some time exhibit two particle class sizes i and j, with corresponding concentrations n_i and n_j. The rate of collision between these two particles is defined as,

$$J_{ij} = k_{ij} n_i n_j \tag{27}$$

Where k_{ij} is a second order collision frequency constant whose form depends on the particle transport mechanism and particle sizes. Next, it is assumed that every collision between particles results in particle of size class k such that k = i + j. Though the collision of two solid particles would not result in sphere, the coalescing drop assumption that class k particles are spherical is required for further derivations of k_{ij} [101].

2.8.7 Collision Frequency Constant Dependence on Transport Mechanism

Depending on the mechanism for particle transport, k_{ij} can vary substantially. There are three forms of transport considered: Perikinetic, Orthokinetic, and Differential Settling. Perikinetic aggregation refers to Brownian motion. Orthokinetic aggregation considers transport from shear originating from stirring or by a flow. Differential settling accounts for collisions which arise during the sedimentation process. Table 3 defines k_{ij} for each of these aggregation mechanisms.

Table 3. Collision Frequency Definitions [104]

Transport Mechanism	$\mathbf{k_{ij}}$
Perikinetic	$\frac{2kT}{3\mu}\frac{\left(a_i + a_j\right)^2}{a_i a_j}$
Orthokinetic	$\frac{4}{3}G\left(a_i + a_j\right)^3$
Differential Settling	$\left(\frac{2\pi g}{9\mu}\right)(\rho_s - \rho)\left(a_i + a_j\right)^3(a_i - a_j)$

In table 3, k is the Boltzmann constant, T is the temperature (K), μ the viscosity of the liquid medium, a_i the radius of class i particles, G is the shear rate, g is acceleration due to gravity, ρ_s is the density of particles, and ρ is the density of the medium. The size of the particles in question has a strong influence on which of the mechanisms is most relevant to aggregation. Past work [104] provides an example of the prevailing mechanism as a function of size.

2.8.8 General Dynamics Equation (Aggregation Specific Population Balance)

The general dynamics equation (GDE) accounts for all particle collisions between size class i and k [104].

$$\frac{dn_k}{dt} = \frac{1}{2}\sum_{i+j\,\rightarrow\,k}^{i=k-1} \alpha k_{ij}\, n_i n_j - n_k \sum_{k=1}^{\infty} \alpha k_{ik} n_i \tag{28}$$

For simplification of the GDE, it is assumed all collisions result in irreversible aggregation such that the collision rate is equal to the aggregation rate and therefore the collision efficiency (α) is unity. In practice, α is less than one due to colloidal and hydrodynamic interactions. Integrated forms of the GDE accounting for collision efficiencies equal to and below one are available in [104], but are reliant on transport specific assumptions.

2.9 Crystal Growth and Dissolution

Though the PBE is written in terms of crystal growth, the equations used to describe that growth are discussed together with dissolution as historically no difference exists in their model expressions. P recovery has been the driving force for the advancement of struvite precipitation technologies. In the pursuit of implementing these systems quickly little discussion has been given to the implications of reactor failure or upset resulting in the generation of fine particles. In a system like the Ostara Pearl where solids recovery is partially dependent on sedimentation, the potential for fines escaping from the reactor is high considering the size of freshly nucleated particles. Given the reports of fines in Pearl systems discussed earlier, the dissolution kinetics of struvite are clearly relevant to the success of P precipitation systems in the future. Without knowing the dissolution kinetics of struvite, it is impossible to make meaningful engineering decisions regarding implementation or the necessity of fines reduction strategies.

Understanding the dissolution kinetics of sparingly soluble salts is a common research topic in environmental engineering where many natural materials are considered sparingly soluble. However, as [106] notes, a disagreement in the correct approach to modelling dissolution is present in the field. This disagreement stems from the basis upon which you derive the governing equations for dissolution. Since the introduction of transition state theory [29] the commonly accepted notion was that dissolution directly mirrored precipitation, but with the reverse reaction. This led to introduction of equations of the form [85], [106],

$$\frac{dC}{dt} = k\frac{A}{V}(K_{sp} - \prod C^{z}) \tag{29}$$

Where C is the concentration of a constituent ion, z is the stoichiometric coefficient of C, k is the dissolution rate constant, A the surface area of the solute, and V is the volume of the solvent. Studies on the dissolution of calcite, quartz, and dolomite have often taken this form or one similar in respect to the order of the equation (order $\neq 1$) [107]–[110].

Other attempts have been made at relating dissolution rate to the physical pitting phenomena observed in dissolution studies with AFM [106], [111], [112]. These works aim to explain the "long tails" observed by [113]. Similar to how some slightly saturated solutions do not form precipitate because of the statistical nature of nucleation, it has been observed that for non-ideal solutes undersaturated solutions do not always induce dissolution [111], [113]. Introduction of a new term "critical radius" by [111] explains slowing of dissolution not captured by transition state theory. While evidence is given by [111] that critical radii are of particular importance to dissolution of fine particles, this concept is outside of the scope of this work.

Following the strict empirical kinetics basis argued by [106] the derivation of the dissolution rate equation, known as the shrinking object (SO) model, is first order with respect to a single species in the mineral of interest,

$$\frac{dC}{dt} = k\frac{A}{V}(C_{sat} - C) \tag{30}$$

Here C and C_{sat} are the concentrations of dissolved magnesium, ammonium, or ortho-phosphate in solution and at equilibrium, respectively. While the purpose of this work is not to argue which equation is most correct the SO model lends itself to empirical work more readily than the equation derived from transition state theory and therefore will be used here. Secondly, for the fines which are of concern in the Ostara Pearl, a model which can account for particle size changes is likely necessary. Given that so little mass is present in the fines generated, most particles will likely shrink to some degree or completely dissolve. The SO model is aptly named for its purpose – the model was developed for cases in which the size of the solute changes during dissolution [114]. While the assumption of spherical geometry is used in this work, derivations of the SO model for other geometries exist [115], [116]. By integrating equation 30 a linearized expression is created under the assumption of constant A and V,

$$-\ln\left(1-\frac{C}{C_{sat}}\right)=k\frac{A}{V}t \tag{31}$$

This expression can then easily be used to determine the dissolution rate constant from empirical concentration time-series data. Some work has shown a need for another parameter related to shear be included in dissolution rate equations [107]. For sparingly soluble salts the dissolution is assumed to be surface controlled and will have minimal difference attributed to high shear [117]. Though it has become commonplace to consider crystal growth and dissolution equal and opposite processes for simplicity in modelling, this work strives to provide a model parameter (dissolution rate constant) that is an intrinsic property of struvite. Rather than lumping rate constants with an extrinsic property such as total solute mass or surface area, this work provides a basis upon which future researchers can accurately base their modeling on regardless of the morphology of the source material in question. This work also strives to open a discussion on whether the PBE necessarily requires a secondary dissolution term which does not abide by the assumptions taken by the current crystal growth expression.

2.10 Understanding of Struvite Crystallization is Limited

Struvite crystallization is a technique that has been proven to efficiently convert soluble P to a solid recoverable form. Brought on by regulatory pressure, the implementation of struvite crystallizer reactors at full scale has been quick and with little regard for the possible implications of reactor upsets or even normal operation that can produce large fractions of fines.

Modelling of struvite crystallizers likewise has ignored dissolution due to the difficulty in predicting particle size distributions in real-time while accounting for all the different processes involved in crystallization.

Studies which focus on individual parts of the PBE are required to further our understanding of the crystallization of struvite. This study works to fill the posed lacuna in the dissolution kinetics of fines generated in struvite crystallizers. In combination with plant-wide modelling, an understanding of the value of struvite crystallizer technologies is furthered and helps inform future WRRFs of the benefits of the technology.

CHAPTER 3: MATERIALS AND METHODS

To determine the dissolution rate constant of field grown struvite short-term dissolution tests were performed and fit using the shrinking object model. Particles of different sizes but from the same source were used to determine the influence of size on dissolution in the short-term studies as well. Long-term dissolution studies at multiple temperatures were used to determine the concentration of P at saturation. Ion chromatography (IC) and inductively coupled plasma optical emission spectroscopy (ICP-OES) were used to experimentally determine solution chemistry. Morphology and chemical heterogeneity of the solids was determined using a scanning electron microscope (SEM) equipped with energy dispersive x-ray spectroscopy (EDS). To elucidate physical and chemical differences in dissolution behavior observed between particles, x-ray diffraction (XRD) and fourier transform infrared spectroscopy (FTIR) were used on liquid and solid samples.

3.1 Field Grown Struvite Samples and Preparation

Multiple sources of field grown struvite seeds were tested in this study. Following the convention of struvite seeds produced in Ostara Pearl® reactors, particles of a diameter, D, are named according to equation 32.

$$SGN\,X = D\,(mm) * 100 \tag{32}$$

Future references to the various samples will be in the form Source SGN D. When necessary an identifier A/B will be added when referencing a single run from a set of duplicate experiments.

The first set of samples tested was from the Clean Water Services (CWS) Durham facility in Tigard, Oregon. These samples were generated in an Ostara Pearl reactor with struvite particle diameters ranging from 4.5 mm (SGN 450) down to a mix sized dust that passed a 350 µm sieve (dust).

The second set of samples were from an Ostara Pearl reactor at the Stickney Water Reclamation Plant in the Metropolitan Water Reclamation District of Greater Chicago in Chicago, Illinois. The struvite particle diameters ranging from 3.0 mm (SGN 300) down to a mixed size dust that passed a 350 µm sieve (dust).

The final set of samples was from an AirPrex pilot reactor at the Metro Wastewater Reclamation District (MWRD) in Denver Colorado, which generated particles with a 125 µm diameter. Sand was present in these samples as part of the AirPrex process.

All seeds were degassed at 40 °C and ambient pressure for two weeks to remove volatile organics without decomposing struvite.

3.2 Reference Solids

Reference struvite (98%; Alfa Aesar) and hydroxyapatite (For analysis; Acros Organics) were used as control samples to determine equilibrium behavior of pure solids. Attempts were made to sieve these reference solids to determine particle size for future kinetics studies, but the hygroscopic nature of the samples resulted in clumping during sieve analysis.

3.3 Buffer Solution Preparation

The following method was used to prepare 10 L of 500 mM tris(hydroxymethyl)aminomethane (tris) buffer at pH 7.5. First, 605.7 g of tris was partially dissolved in 9.5 L of DI water. Next, 350 mL of concentrated hydrochloric acid (HCl 37% w/w) was added to adjust pH down to a target of 7.5 ± 0.02 arbitrarily fixing the ionic strength of the solution to 0.45 M. A silver free double junction electrode (Orion ROSS Ultra Refillable pH/ATC Triode Combination Electrode) was used to check pH to eliminate the possibility of Ag-tris precipitate forming in the frit. The solution was allowed to cool overnight to limit any differences in buffering capacity of tris at higher temperatures caused by acid dilution. An additional 150 mL of DI water was added to reach 10 L. The solution was then allowed to equilibrate for at least 1 week before use.

3.4 Dissolution Experiments

3.4.1 Short Term Dissolution

Short-term dissolution tests were conducted to determine the dissolution rate constant of the various solids tested through fitting the increasing concentration of PO_4^{3-} to the shrinking object model. The solids described in *3.1* were tested in duplicates in a short-term batch dissolution experiment following the same protocol for each solid tested. A 500 mL three-neck flask (figure 2) was first triple rinsed in DI water, followed by a HCl acid rinse, and finally a tris buffer rinse. Then, the flask was filled with 450 mL of 500 mM tris buffer (prepared as described in *3.3*). A sampling needle and a calcium ion selective electrode (Sension+ 9660 Calcium ISE) were inserted into separate outer flask necks and sealed with air-tight silicone stoppers. The solution was then sparged with N_2 and mixed with a magnetic stir bar for 10 minutes to remove any dissolved CO_2. The pH of the solution was checked at the beginning and end of experiments to ensure a pH of 7.5

± 0.02 was maintained. An initial 2 mL sample was collected before solids addition to account for any residual P in the vessel from previous experiments. Residual P was minimal in all cases and did not affect the results of these experiments.

Each experiment began with the addition of struvite particles to the reaction vessel. Solids were added to the dissolution vessel at a 10 g/L loading to ensure that total particle surface area is nearly constant over the course of the experiment satisfying the constant surface area condition of equation 31. The vessel was then completely closed to the atmosphere by plugging the central neck with a thermometer in a rubber stopper and mixed with a magnetic stir bar at a rate of 300 RPM. A 2 mL sample was collected at 10 minute intervals for 60 minutes starting at t = 0 min. Over the course of the experiment, only 16 mL are removed ensuring V is nearly constant ($\Delta V < 4\%$) therefore satisfying the constant V assumption of one condition of equation 31. Each sample was filtered with a 0.22 μm filter and analyzed for inorganic phosphate using IC. Near real-time (5 sec

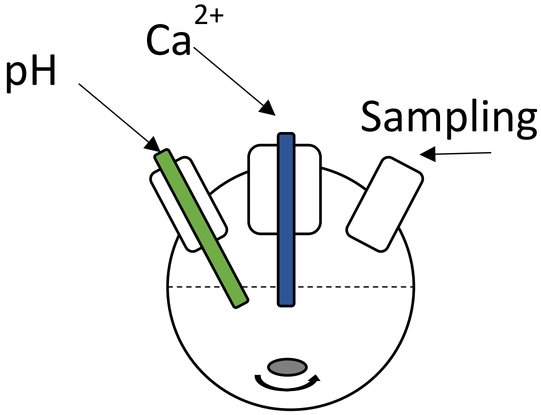

Figure 2. Short-term dissolution apparatus. The pH probe is only inserted at the beginning and at the end of short-term dissolution experiments and is sealed otherwise.

intervals) free calcium (Ca^{2+}) concentrations were monitored using the previously described calcium ion selective electrode (Sension+ 9660 Calcium ISE).

3.4.2 Long Term Dissolution

The equilibrium behavior of the solids of interest was studied using a long-term dissolution experiment at various temperatures. The resulting supernatant solution of the long-term dissolution experiments was analyzed for Mg, Ca, Fe, K, P with IC and ICP. The presence of these ions at equilibrium was used to determine the driving force for dissolution of struvite and other potential co-precipitants in the field grown seeds. Using the same buffer as described in 3.3, 10 g of solids were placed in a 50 mL centrifuge tube and filled to the 45 mL mark in duplicates. Samples were held at three different temperatures: 4, 21.5, and 37 °C for at least 4 weeks. Each tube was manually shaken weekly to limit any diffusional resistance to dissolution. After the last manual mixing at 4 weeks, the samples sat undisturbed for 24 hours to allow particle sedimentation, after which a 750 µL liquid sample was drawn for IC analysis. For CWS SGN 35-450, long-term dissolution experiments were performed between 4.4 °C and 29.5 °C. For CWS dust, all Stickney samples, and MWRD 12.5 long-term dissolution was performed only at 21.5 °C. Note that these experiments will have a slight difference in equilibrium to the short-term experiments because of dissolved CO_2 present in the long-term samples. Though it would be possible to approximate degassed conditions using solution chemistry software, assumptions on the concentration of cations in solution would be necessary. To circumvent this, ICP was used to characterize Ca, Mg, Fe, K, and P in solution. These elements were chosen to account for any calcium phosphates, struvite and K isomorphs, and iron phosphates. Visual MINTEQ 3.1 was used to simulate the solution chemistry at equilibrium in the dissolution reactor. This step was necessary to estimate

C_{sat}. In these simulations, it was assumed the equilibrium behavior of the field recovered seeds would mirror pure struvite. Due to the use of Tris buffer, an entry was added to the Visual MINTEQ 3.1 component library to model the following reaction (equation (33). The equilibrium constant of this reaction was 8.074 [6].

$$Tris + H_3O^+ \leftrightarrow HTris^+ + H_2O \tag{33}$$

3.5 Analytical Techniques

3.5.1 Calcium Ion Selective Electrode

In the short-term dissolution experiments, a calcium ISE (Sension+ 9660C Calcium Combination Ion Selective Electrode) was used to determine the concentration of free calcium (Ca^{2+}) in solution. Data points were collected in 5 second intervals for the full experiment duration. A calibration curve was generated using 0.05, 0.1, 0.5, 1, 5, and 10 mM $CaCl_2$ dissolved in the buffer described in *3.3* (figure 3). Results not shown for this data set as measured calcium concentrations were low in agreement with ICP data.

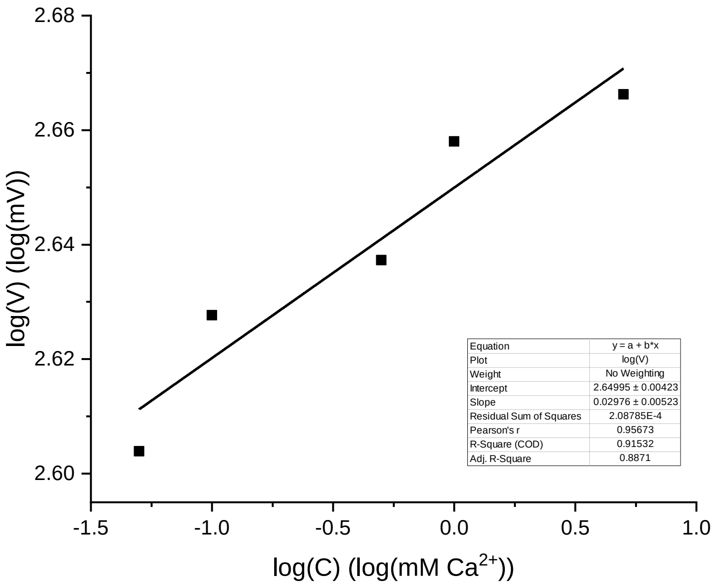

Figure 3. Calibration curve for Ca probe.

3.5.2 Ion Chromatography

The concentration of inorganic phosphate in liquid samples drawn from short- and long-term dissolution experiments was quantified using IC (Dionex ICS-2100) with a Dionex IonPac AS18 column. Samples were diluted 1:1 with DI water and held in a 2 mL IC vial. A calibration curve was generated using a Dionex Combined Five Anion Standard for IC at 5 dilutions (figure 4). This standard contained 25 mg/L F^-, 30 mg/L Cl^-, 100 mg/L NO_3^-, 150 mg/L PO_4^{3-}, and 150 mg/L SO_4^{2-}.

The standard was diluted at the following rates: no dilution, 1/2, 1/10, 1/20, 1/100. This corresponds to orthophosphate concentrations of 150, 75, 15, 7.5, and 1.5 mg/L PO_4^{3-}.

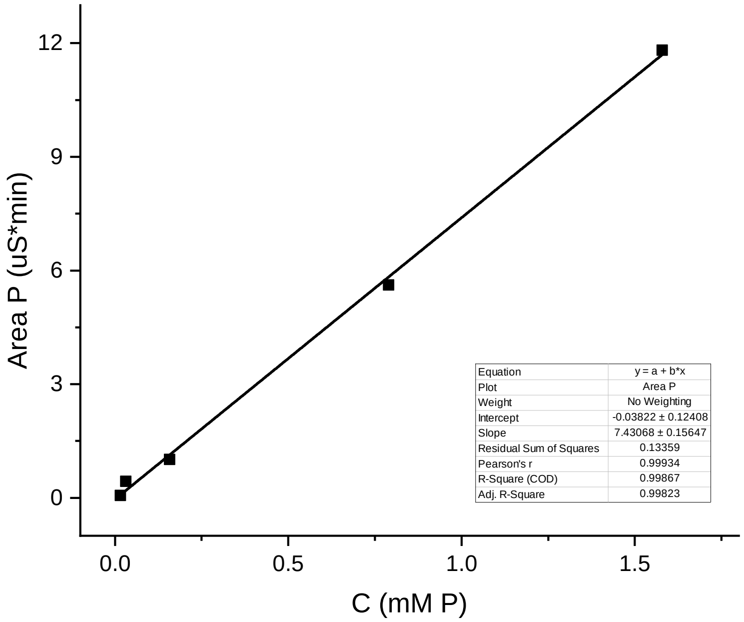

Equation	y = a + b*x
Plot	Area P
Weight	No Weighting
Intercept	-0.03822 ± 0.12408
Slope	7.43068 ± 0.15647
Residual Sum of Squares	0.13359
Pearson's r	0.99934
R-Square (COD)	0.99867
Adj. R-Square	0.99823

Figure 4. Calibration curve for P measured with IC.

3.5.3 Powder X-ray Diffraction

XRD analysis was used to identify crystalline compounds found in the solids tested. All solids were crushed manually in a mortar and pestle to produce fine particles necessary for powder XRD. The diffractometer (Siemens/Bruker D-5000) used was set to scan 1°/min from 10-50° 2θ and did not rotate the sample during analysis. This diffractometer used Cu Kα radiation.

3.5.4 Scanning Electron Microscopy and Electron Dispersive Spectroscopy

An SEM (Hitachi S-4700) was used to determine seed surface and cross section morphology. No conductive coating was needed to image the field grown struvite seeds once the previously described degassing procedure was performed. Without the degassing procedure, significant charging and degassing within the SEM occurred. Cross sections of field grown struvite seeds were created by simply cleaving seeds with a razor. EDS was used to determine the chemical homogeneity of both the seed surface and cross section. No quantitative analysis was done, but qualitative observations were made on the distribution of Mg, Ca, K, and Fe. Acquired SEM images are not shown in this work as no features of interest were seen.

3.5.5 Fourier Transform Infrared Spectroscopy

FTIR (Perkin Elmer Frontier) was used to determine the moieties present that may alter the dissolution rate of the field grown struvite. The analysis was run from 400-4000 cm^{-1} with 8 accumulations per wavenumber. The surface of the field grown struvite was analyzed by direct contact with the detector cell while a powdered sample gave information on the chemistry within the seed. Liquid samples from the long-term dissolution studies were analyzed using FTIR to determine the identity of water-soluble organics that dissolved with struvite.

3.5.6 Inductively Coupled Plasma Optical Emission Spectroscopy

ICP analysis (PerkinElmer Optima 8300) on CWS, Stickney, and MWRD long-term dissolution samples was conducted by the Microanalysis Laboratory at the University of Illinois at Urbana-Champaign. Analytes considered in the analysis were Mg, Ca, K, Fe, and P.

CHAPTER 4: RESULTS AND DISCUSSION

4.1 Determining the Dissolution Rate of Field Grown Struvite

4.1.1 Short-term Dissolution Experiments

The time-series P concentration data obtained through the short-term dissolution experiments provides quantitative insight into the dissolution behavior of the field recovered struvite (figure 5). For both CWS and Stickney, the fastest dissolution and resulting increase in P was seen in dust samples with the exception of CWS SGN 35 which was faster. The slowest to dissolve was SGN 450 and SGN 300 for CWS and Stickney respectively. Based on the SO model (equation 30), the faster dissolution of small particles observed was expected as the total solute surface area increases at the same mass loading. What was not expected was the substantial increase in the final P concentrations measured for CWS SGN 35 as compared to other struvite from CWS, the reference struvite, and equilibrium model estimates for C_{sat} (figure 5 A). Experimentally, the reference struvite reached 6.14 mM P after 60 min (data not shown) compared to the 5.84 mM theoretical P calculated by VMinteq. A small increase in final P was measured for both Stickney dust and MWRD 12.5 as compared to other samples from Stickney and the reference struvite. Though this does seem to indicate compositional differences between the seeds with higher solubility as compared to the rest, this data set only represents the first 60 minutes of dissolution and may not accurately reflect equilibrium behavior. Other species such as organic ligands or metal cations may be present artificially increasing the solubility of struvite. Alternatively, other P containing solids may be dissolving in conjunction with struvite. The differences seen between dust samples at CWS and Stickney indicate that the source of the solids (and resulting source specific composition) may be a larger factor than size when considering equilibrium chemistry.

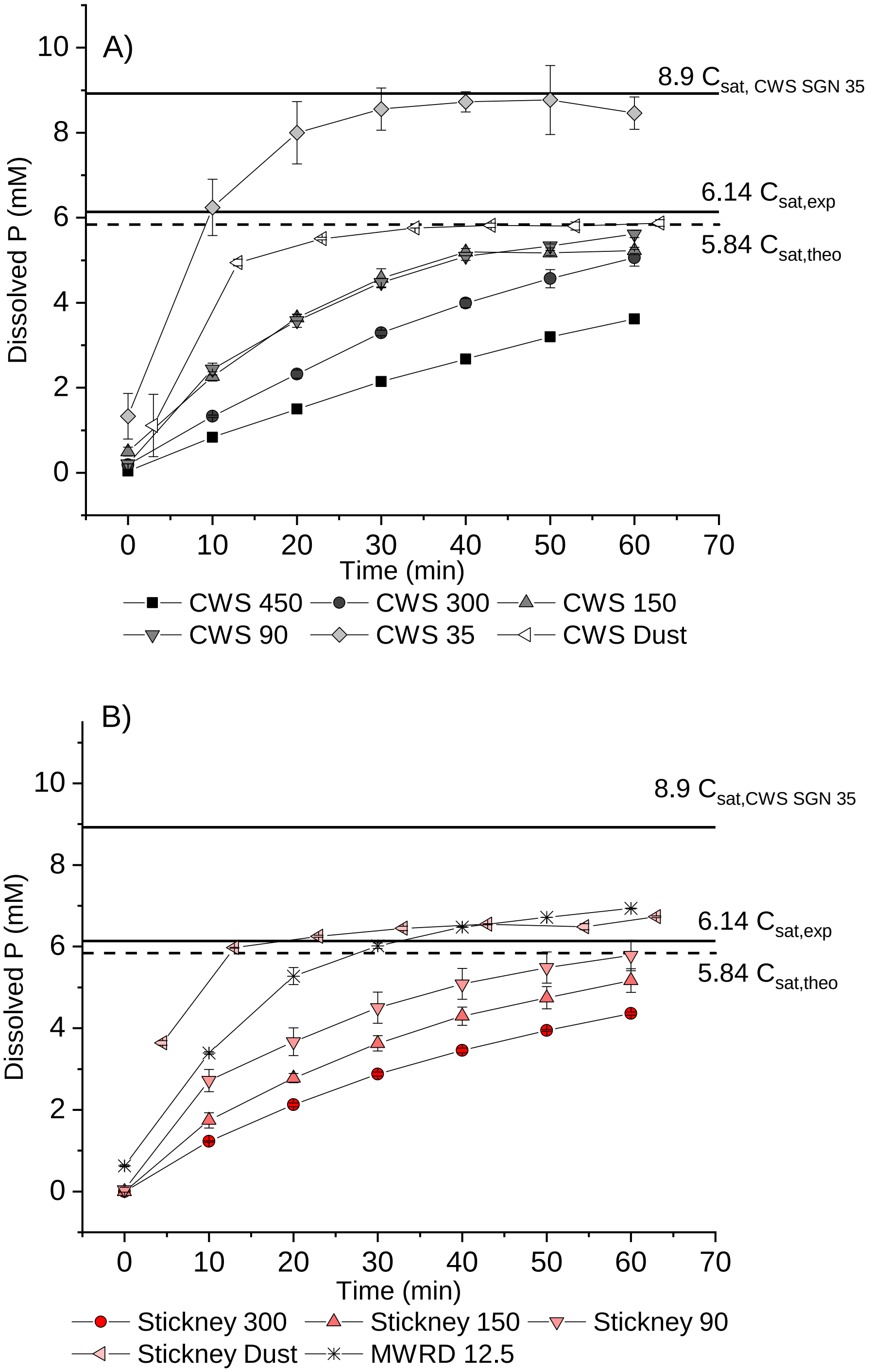

Figure 5. P release during short-term dissolution experiments for A) CWS and B) Stickney and MWRD field recovered struvite.

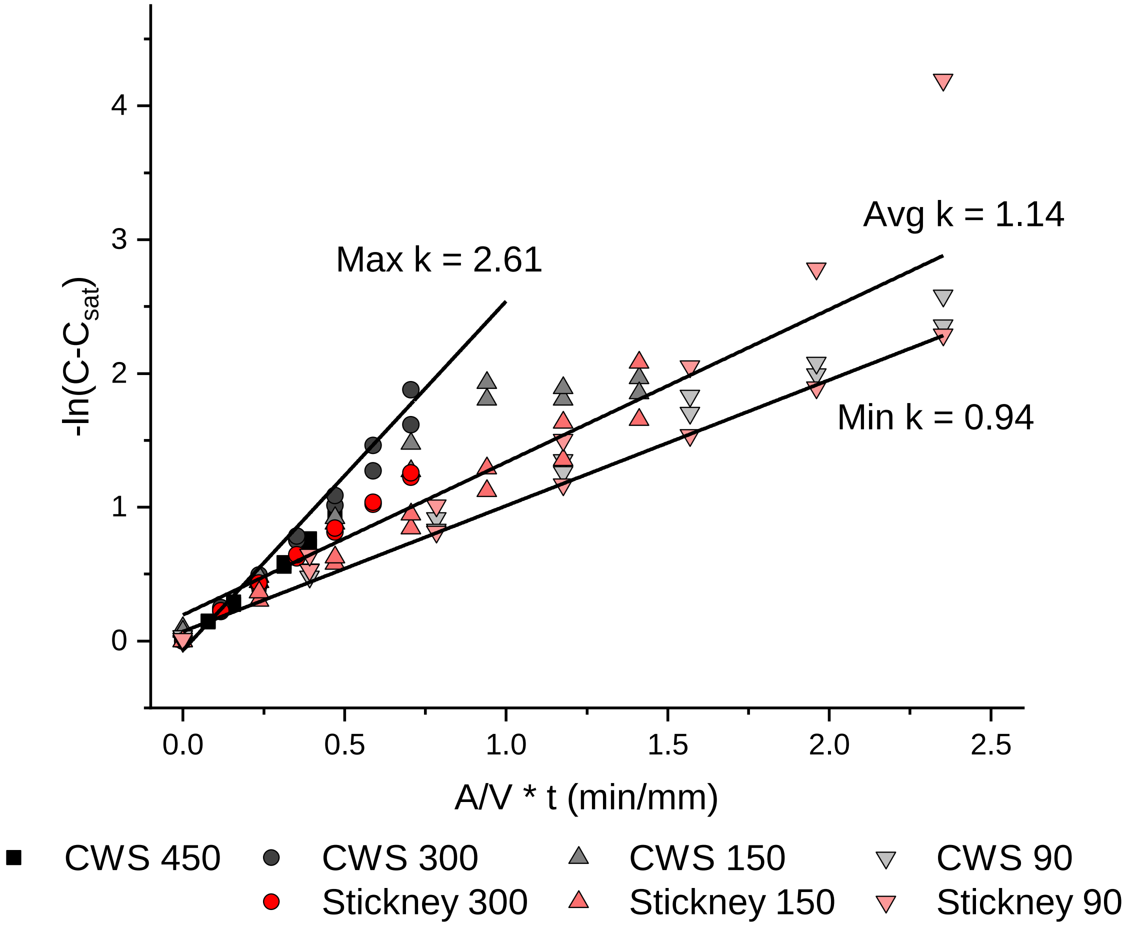

Figure 6. Data from figure 5 fit to the linearized shrinking object model. The slope of the fits shown are the dissolution rate constants (mm/min). A fit is given for the entire data set (Avg k), slowest k (Stickney SGN 90 A), and fastest k (CWS SGN 300 B).

The P concentration time-series data from figure 5 was fit to the linearized shrinking object model (equation 31), as shown in figure 6. The slope of the fit lines in figure 6 are the dissolution rate constant of the field grown struvite recovered at CWS and Stickney. By fitting the entire data series, a dissolution rate constant of 1.14 mm/min was found. A weak correlation was found between particle size and the rate constants derived from individual data series shown in figure 11. This correlation is potentially related to hydrodynamic differences experienced by the different sized particles in the reactor in contrast to that experienced by [117]. Though a shear rate was not calculated for this system, upon visual inspection during the short-term dissolution experiments mixing lead to a more homogenous mixture as particle size decreased. To reconcile the spread of k values seen in figure 11 with a need for a single value for modeling purposes, a minimum and maximum dissolution rate constant was given for the fastest and slowest dissolving solids observed, k = 0.94 mm/min from Stickney SGN 90 A and k = 2.61 mm/min from CWS SGN 300 B. As the objective of this work was only partially to elucidate an exact value for the dissolution rate constant of field grown struvite, a range of dissolution rate constant values is more useful in providing a basis for uncertainty analysis in future plantwide studies.

In figure 6, CWS SGN 35, both CWS and Stickney Dust, and MWRD 12.5 are not included. These were excluded from the series because an accurate surface area calculation was not possible (Dust) and measured concentrations of P exceeded the C_{sat} of the remaining samples for a majority of the test period (CWS SGN 35, Stickney Dust, and MWRD 12.5). By adjusting the C_{sat} used in equation 31 to 8.9 mm P and 7.1 mM P, a dissolution rate constant of 0.55 mm/min and 0.21 mm/min was found for CWS SGN 35 and MWRD 12.5 respectively (figure 7). The adjusted values for C_{sat} were based on the apparent C_{sat} seen in figure 5. Attempts at estimating surface area of the dust particles through sieve analysis were not successful due to the hydrophilic nature of the fine solids leading to clumping. Because of this only a less rigorous analysis which lumped together the dissolution rate constant with surface area was possible for CWS and Stickney Dust shown in figure 12. Though this type of analysis is not ideal because it produces a lumped dissolution rate constant that is specific to the solid in question and difficult to compare to other studies, it is reminiscent of precipitation studies where little concern is given to the surface area of the solids in the crystallization reactor.

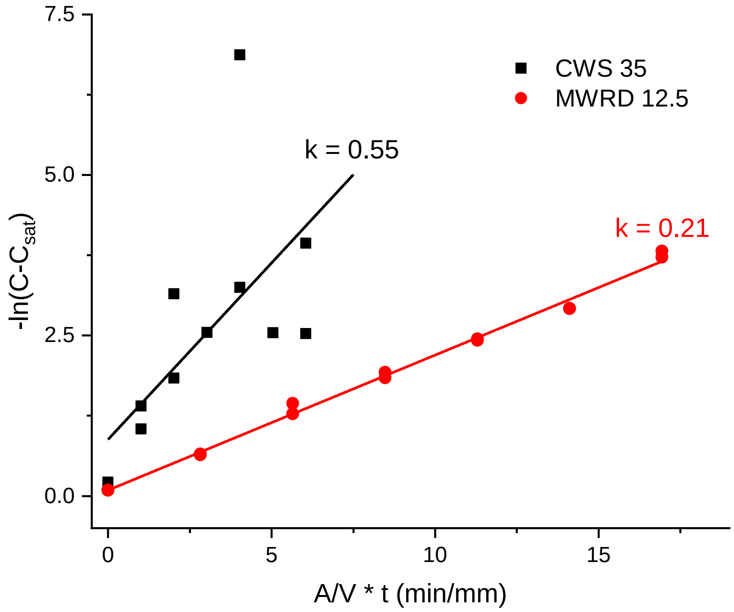

Figure 7. CWS 35 and MWRD 12.5 fit to the linearized shrinking object model.

4.1.2 Long-term Dissolution Experiments

Though the original intent of this study was to use the P concentrations measured in the long-term experiments as C_{sat} in the calculation used in figure 6, a comparison and mismatch between the concentrations of P measured in long-term dissolution experiments in both IC and ICP with the concentrations of P measured in short-term experiments showed this was not possible (Tables 4 and 5). At the point of collection of samples for IC and ICP a distinct acidic odor was present potentially signifying biological activity and P removal through growth. Regardless of any biological activity, the odor could indicate a high concentration of organics leached from the struvite seeds resulting in a different solution chemistry than what was tested in short-term dissolution experiments. Though the concentration of P determined by ICP did not match short-term experiments (Table 5) the results are still useful in comparing relative abundance of struvite constituent ions to other impurity ions (Ca, K, Fe). Near parity was seen in all samples in terms of

Mg:P mirroring the stoichiometry of struvite. Less than 0.03 mM Fe, 0.2 mM Ca, and 0.06 mM K was seen in all cases.

4.1.3 Overall Dissolution Rate Estimates for Plantwide Process Modeling

Using the dissolution rate constants derived from figure 6, an estimate for expected overall dissolution rate at a WRRF as a function of struvite diameter is possible. Figure 8 assumes the chemistry of the dissolving solids is similar to pure struvite such that C_{sat} = 6.14 mM P, the solids were returned to the headworks of the WRRF where the solution concentration is low that $(C_{sat}-C) = C_{sat}$, mixing rates in the headworks are similar enough to these experiments such that the range of k's used is valid, a mass loading of 10 mg/L, and total volume of 850 m^3. Figure 8 shows particle size is of great importance when estimating the dissolution rate of field grown struvite lost from a crystallizer. Negligible dissolution is expected at the given conditions for particles with diameters of 100 μm regardless of the dissolution rate assumed. However, for particles less than 10 μm, dissolution rapidly increases past 0.1 mM P/min and for 1 μm particles between 0.2-0.55 mM P/min is estimated. As the particles returned to the headworks become smaller, more uncertainty is present in the dissolution rate due to uncertainty in the dissolution rate constant. Though these estimates alone cannot determine the impact of fines dissolution on plantwide performance, the particle size distributions reported [21], [31], [82], [118] and modelled [31], [82] thus far in crystallizer reactors seems to indicate fines generated are well within the higher dissolution rate regimes shown here by size.

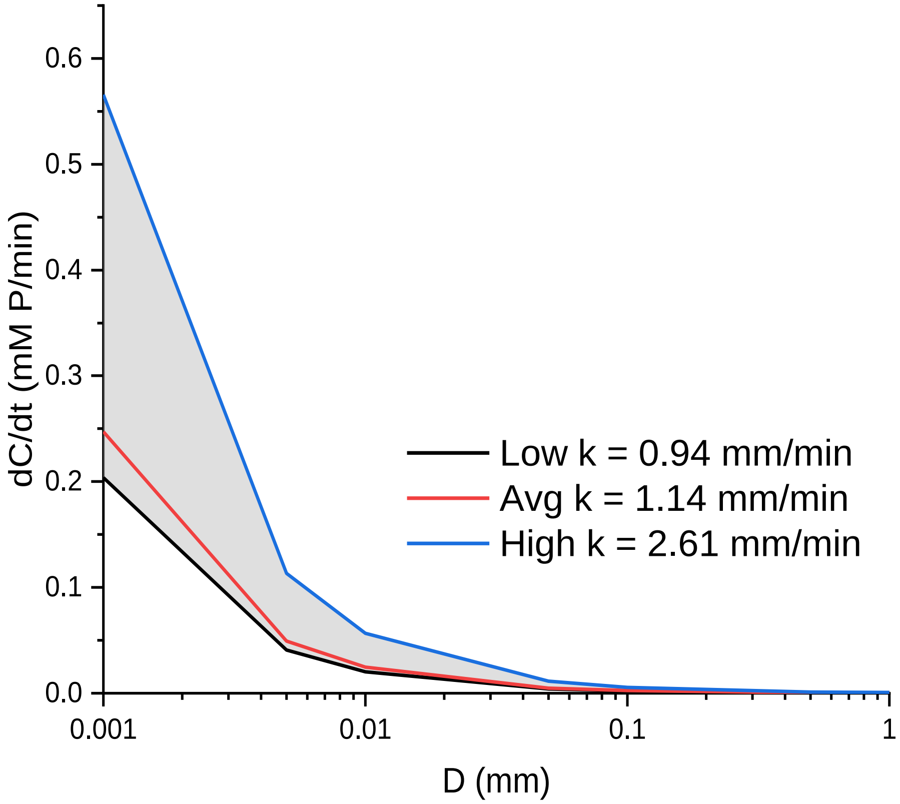

Figure 8. Estimated dissolution rates for field grown struvite at a WRRF. Total volume is 850 m^3 at a mass loading of 10 mg P/L.

4.2 Elucidating the Physical and Chemical Differences of Field Grown Struvite

Differences in the crystallographic nature of the solids which were more soluble than expected in the short-term dissolution experiments were observed in XRD spectra shown in figure 9. In CWS SGN 35 three extraneous peaks were detected at 10.2°, 18.8°, and 24.5° and identified as dittmarite ($MgNH_4PO_4*H_2O$). In Stickney dust dittmarite peaks were found at 10.2° and 18.8°. MWRD 12.5 was more complex with a dittmarite peak at 27.6°, a quartz peak at 26.7°, and an unidentified but strong peak at 47.38°. The quartz impurities in MWRD 12.5 are expected due to the sand used as a seed material in the precipitation of the sample. All other samples were nearly identical to the struvite reference solid with some slight peak shifting attributed to strain within the crystals (figure 13 A and B). No significant peak matches were made with reference hydroxyapatite in any of the field grown samples.

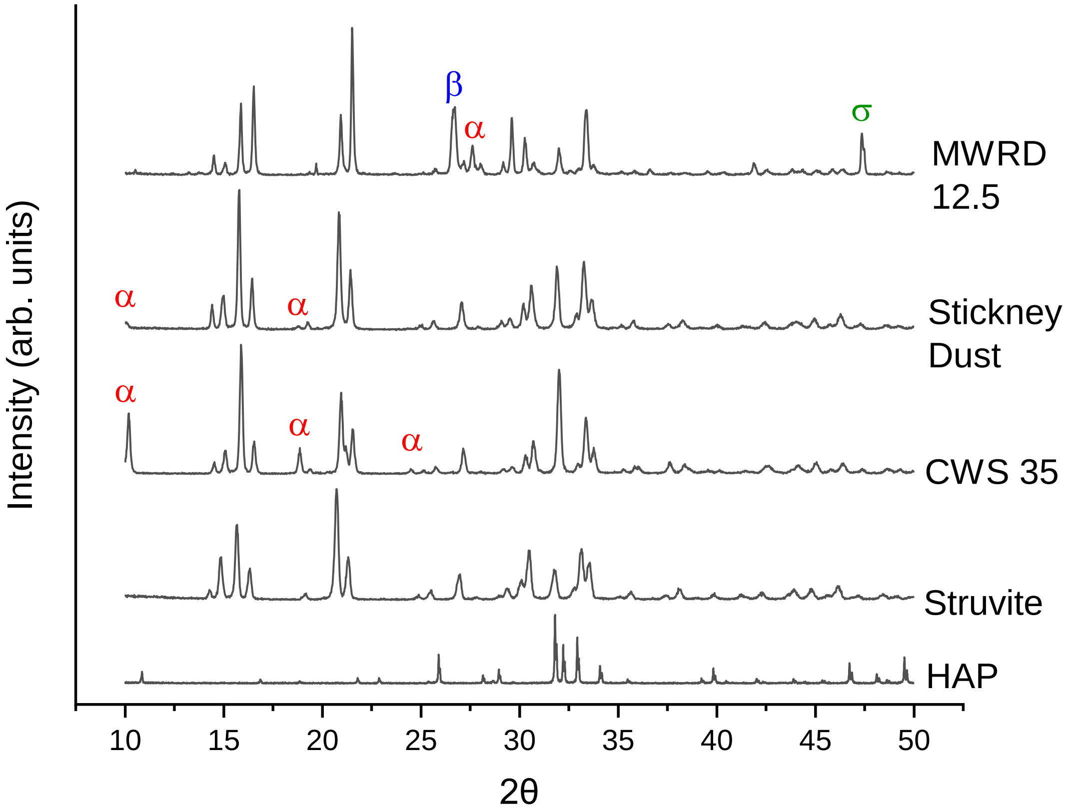

Figure 9. XRD of solids which featured distinct crystalline phases other than struvite. These solids are the solids which exhibited increased P solubility seen in figure 5. Characteristic peaks are marked as follows Dittmarite – α, Quartz – β, and Unidentified – σ.

Differences were also observed in the FTIR spectra of the solids studied as shown in figure 14. In this analysis the objective is not to find specific compounds which may be present in the samples through fingerprint analysis. Rather, we strive to show common group frequencies shared within the samples and contrast that with the reference struvite sample to understand what types of molecules may alter dissolution behavior from pure struvite either through molecules adsorbed on the surface of the field recovered struvite or in solution acting as a dissolution inhibitor. Liquid samples drawn from the long-term dissolution experiments provide solution chemistry information, crushed samples give general chemistry of the solid, and “solid” samples give surface character. As a baseline for comparison, the liquid reference struvite sample was relatively uneventful with only a weak and broad absorbance at ~3200 cm^{-1}. This could correspond to a primary amide or amine though both have absorbance bands near 3400-3300 cm^{-1} are not seen in the liquid fraction spectra [119]. As a reference sample, the pure struvite is expected to contain only inorganic PO_4^{3-} (very strong at 1030 cm^{-1} and medium at 570 cm^{-1}) and NH_4^+ (strong at 1410 cm^{-1}) FTIR bands [119], [120]. In fact, the reference does contain inorganic IR bands at 1430 cm^{-1} and 560 cm^{-1}. However, medium strength broad peaks also appear at 2330 cm^{-1}, 2870 cm^{-1}, 3220 cm^{-1}, and very weakly at 3500 cm^{-1} strengthening the indication of a primary amine (doublet 3380 and 3300, strong peak 3000-2700 cm^{-1}) seen in the liquid fraction or of a secondary amine (broad strong peak 2700-3000 cm^{-1}, medium-weak peak at 1620-1560 cm^{-1}) [119].

For the CWS SGN 450 – 90 no noticeable difference compared to the struvite standard is seen in the FTIR spectra of liquid and solids samples. CWS Dust liquid seems to lack some of the broad 3400 cm^{-1} band, but the liquid and solid is otherwise identical to the reference struvite. The liquid sample of CWS SGN 35 seems to more closely mirror the solid reference struvite spectra with the exception of peaks in the fingerprint region 1650-1450 cm^{-1} and an absence of peaks below 960 cm^{-1}. Crushed CWS SGN 35 was nearly identical to the reference struvite spectra. The surface sample of CWS SGN 35 was very distinct from the reference struvite spectra with a weak peak at

3420 cm^{-1}, a doublet at 2900 cm^{-1} and 2750 cm^{-1}, and a distinct fingerprint region (figure 10). This could describe again describe a primary amine by fulfilling 3500-3300 cm^{-1}, 3400-3200 cm^{-1}, 1630-1590 cm^{-1}, 900-600 cm^{-1} [119].

Stickney SGN 300 – 90 is characterized by a lack of bands in the liquid spectra and similar inactivity in the solid spectra until ~1500 cm^{-1} where weak peaks appear where the strong reference solid peaks are present. Stickney dust is similar in the solid and liquid, but the crushed sample is distinct (figure 10). The crushed sample only exhibits a weak peak at 1000 cm^{-1} and 570 cm^{-1}. Any definitive conclusions are hard to draw from this sample in terms of what the fingerprint region indicates, but an absence of upper bands present in the reference struvite is clear.

The MWRD 12.5 sample matches the reference struvite spectra in all three cases.

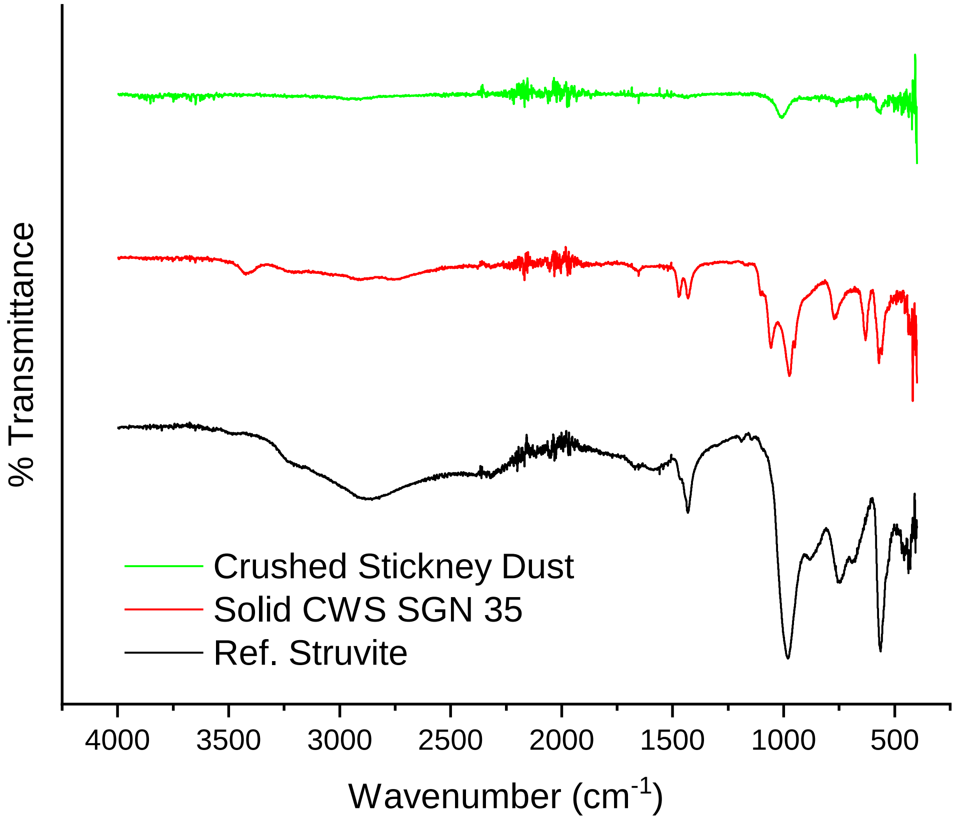

Figure 10. Differences in FTIR spectra from a reference struvite sample in two solids shown to be more soluble than expected in short-term dissolution experiments.

CHAPTER 5: CONCLUSIONS AND FUTURE WORKS

5.1 Conclusions and Engineering Implications

Due to the increased implementation of struvite crystallization systems across the U.S. and in Europe, and the now known presence and washout of fines, a better understanding of the kinetics of dissolution for struvite is necessary for accurate modelling of plantwide processes. The findings of this study will allow for kinetics-based dissolution using the shrinking object model without the need to rely on lumped dissolution rate parameters. This work provides a dissolution rate constant which is an intrinsic property of the struvite studied here. The differences observed even in short-term dissolution experiments indicate that models based on a strict definition of K_{sp} are in some cases accurate as in SGN 90 – SGN 450, others such as that of SGN 35 may severely underestimate the dissolution of struvite. A return to empirical models such as the shrinking object model may be necessary to accurately model dissolution of field grown solids. A very weak correlation between the dissolution rate parameter and particle size was shown, but additional work is needed to confirm the influence of shear on the dissolution rate of field grown struvite. Though a deeper understanding of equilibrium chemistry of these samples was not possible through long-term dissolution studies, relative abundance of other common impurity ions found through ICP showed Ca, K, Fe were all in very low concentrations and not likely the source of enhanced solubility.

Only in samples which exhibited enhanced solubility did a difference appear in the XRD or FTIR spectra compared to reference struvite. Using XRD a dehydrated magnesium ammonium phosphate mineral, dittmarite, was detected in all three higher solubility solids. The presence of this solid was not expected as the Ostara Pearl is designed to operate at WRRF temperatures and not those known to produce the monohydrate [121]. Quartz in MWRD 12.5 was expected as sand is used as seed material in its precipitation. An unidentified peak at 46° 2θ may play a part in MWRD 12.5's enhanced solubility. The FTIR spectra of both CWS SGN 35 and Stickney dust pointed to an importance on characterizing both the surface and internal chemistry of field grown struvite. In the case of CWS SGN 35 it seemed that a surface coating different to the inorganic groups seen in the reference struvite was present. Both functional group bands and the fingerprint region were distinct on the surface from the reference struvite. This type of spectra was not replicated in crushed samples likely indicating a surface effect. For Stickney dust, it appeared as although the surface matched the reference struvite, the crushed sample and therefore the internal chemistry of the dust was not consistent with pure struvite. Limited conclusions can be stated from this result other than a lack of nitrogenous functional groups seemed to be present in the core of Stickney dust potentially enhancing dissolution once the surface of these particles has dissolved.

5.2 Future Works

Future works will focus on the integration of these results into plant-wide modelling to simulate the impact of fines dissolution in other parts of the treatment train based on particle size and saturation concentrations of phosphate. By providing a range of dissolution rate constant values measured empirically, a baseline degree of uncertainty can be accounted for in plantwide modelling giving the model more relevance to plants which have not yet fully characterized the fines generated in their crystallizer in terms of C_{sat} or their dissolution rate constant. More work in highly mixed systems is needed to ensure the weak correlation found between particle size and dissolution rate constant is negligible, and therefore surface controlled in low mix systems like primary clarifiers where fines will be recycled in the WRRF.

As the introduction of crystallizer technologies becomes more prevalent throughout the world, accounting for dissolution of fines could become a necessary part of accurate modelling especially for systems where upsets occur that result in a larger volume of fines [50]. By overloading the headworks with fines, P is essentially dosed in a form that could potentially bypass sedimentation and result in an under-designed EBPR system. This can lead to missing regulatory limits or a need to increase VFA dosing in EBPR to match the additional P removal demand. Both cases could be economically damaging to the WRRF, but as of yet have not been tested with a plantwide costing model. This work in combination with plantwide costing models will inform industry on the net-benefits of crystallizer technologies during optimal and sub-optimal P recovery and determine whether fines capture is necessary or an unwarranted preventative measure.

REFERENCES

[1] A. N. Sharpley, S. J. Smith, O. R. Jones, W. A. Berg, and G. A. Coleman, “The Transport of Bioavailable Phosphorus in Agricultural Runoff,” *J. Environ. Qual.*, vol. 21, no. 1, pp. 30–35, 3/01 1992.

[2] S. R. Carpenter, N. F. Caraco, D. L. Correll, R. W. Howarth, A. N. Sharpley, and V. H. Smith, “NONPOINT POLLUTION OF SURFACE WATERS WITH PHOSPHORUS AND NITROGEN,” *Ecol. Appl.*, Aug. 1998.

[3] P. Cornel and C. Schaum, “Phosphorus recovery from wastewater: needs, technologies and costs,” *Water Sci. Technol.*, vol. 59, no. 6, pp. 1069–1076, Mar. 2009.

[4] P. Heffer and M. Prud’homme, “Fertilizer Outlook 2016-2020,” p. 7, 2016.

[5] D. Cordell and S. White, “Tracking phosphorus security: indicators of phosphorus vulnerability in the global food system,” *Food Secur.*, vol. 7, no. 2, pp. 337–350, Apr. 2015.

[6] N. N. Rabalais, R. E. Turner, and W. J. Wiseman, “Hypoxia in the Gulf of Mexico,” *J. Environ. Qual.*, vol. 30, no. 2, pp. 320–329, Mar. 2001.

[7] D. J. Conley *et al.*, “Controlling Eutrophication: Nitrogen and Phosphorus,” *Science*, vol. 323, no. 5917, pp. 1014–1015, Feb. 2009.

[8] W. M. Kemp *et al.*, “Eutrophication of Chesapeake Bay: historical trends and ecological interactions,” *Mar. Ecol. Prog. Ser.*, vol. 303, pp. 1–29, Nov. 2005.

[9] C. Le, Y. Zha, Y. Li, D. Sun, H. Lu, and B. Yin, “Eutrophication of Lake Waters in China: Cost, Causes, and Control,” *Environ. Manage.*, vol. 45, no. 4, pp. 662–668, Apr. 2010.

[10] L. H. T. Dederen, “Marine eutrophication in Europe: similarities and regional differences in appearance,” in *Marine Coastal Eutrophication*, R. A. Vollenweider, R. Marchetti, and R. Viviani, Eds. Amsterdam: Elsevier, 1992, pp. 663–672.

[11] D. W. Schindler, “Evolution of Phosphorus Limitation in Lakes,” *Science*, vol. 195, no. 4275, pp. 260–262, Jan. 1977.

[12] L. Volterra, M. Boualam, A. Menesguen, J.-P. Duguet, J. Duchemin, and X. Bonnefoy, “Eutrophication and Health,” World Health Organization, 2002.

[13] O. US EPA, “Status of Nutrient Requirements for NPDES-Permitted Facilities,” *US EPA*, 15-Jun-2016. [Online]. Available: https://www.epa.gov/npdes/status-nutrient-requirements-npdes-permitted-facilities. [Accessed: 12-Jul-2019].

[14] “State Progress Toward Developing Numeric Nutrient Water Quality Criteria for Nitrogen and Phosphorus | Nutrient Pollution Policy and Data | US EPA.” [Online]. Available: https://www.epa.gov/nutrient-policy-data/state-progress-toward-developing-numeric-nutrient-water-quality-criteria. [Accessed: 12-Jul-2019].

[15] L. L. Blackall, G. R. Crocetti, A. M. Saunders, and P. L. Bond, “A review and update of the microbiology of enhanced biological phosphorus removal in wastewater treatment plants,” *Antonie Van Leeuwenhoek*, vol. 81, no. 1–4, pp. 681–691, 2002.

[16] T. Mino, M. C. M. van Loosdrecht, and J. J. Heijnen, “Microbiology and biochemistry of the enhanced biological phosphate removal process,” *Water Res.*, vol. 32, no. 11, pp. 3193–3207, Nov. 1998.

[17] C. González-Fernández and P. A. García-Encina, “Impact of substrate to inoculum ratio in anaerobic digestion of swine slurry,” *Biomass Bioenergy*, vol. 33, no. 8, pp. 1065–1069, Aug. 2009.

[18] H. Johannes Pöpel and N. Jardin, “Influence of Enhanced Biological Phosphorus Removal on Sludge Treatment,” *Water Sci. Technol.*, vol. 28, no. 1, pp. 263–271, Jul. 1993.

[19] S. Uludag-Demirer, G. N. Demirer, and S. Chen, “Ammonia removal from anaerobically digested dairy manure by struvite precipitation,” *Process Biochem.*, vol. 40, no. 12, pp. 3667–3674, Dec. 2005.

[20] K. N. Ohlinger, P.E., T. M. Young, and E. D. Schroeder, “Kinetics Effects on Preferential Struvite Accumulation in Wastewater,” *J. Environ. Eng.*, vol. 125, no. 8, pp. 730–737, Aug. 1999.

[21] M. M. Seckler, O. S. L. Bruinsma, and G. M. Van Rosmalen, “Phosphate removal in a fluidized bed—I. Identification of physical processes,” *Water Res.*, vol. 30, no. 7, pp. 1585–1588, 1996.

[22] “Ostara Nutrient Recovery - About,” *Ostara Nutrient Recovery*. [Online]. Available: https://ostara.com/about/. [Accessed: 07-Jul-2019].

[23] “Crystal Green Fertilizer,” *Crystal Green*. [Online]. Available: https://crystalgreen.com/. [Accessed: 07-Jul-2019].

[24] R. Lee, “Doubling Down On Phosphorus,” presented at the CSWEA, Madison, WI, 16-May-2019.

[25] K. N. Ohlinger, T. M. Young, and E. D. Schroeder, “Predicting struvite formation in digestion,” *Water Res.*, vol. 32, no. 12, pp. 3607–3614, Dec. 1998.

[26] S. Agrawal, J. S. Guest, and R. D. Cusick, “Elucidating the impacts of initial supersaturation and seed crystal loading on struvite precipitation kinetics, fines production, and crystal growth,” *Water Res.*, 2018.

[27] A. Romero *et al.*, “Lost Crystals– Impacts of Struvite Recovery Performance on Plant Capacity for Achieving Low-P Effluent.,” p. 6, 2018.

[28] C. Kazadi Mbamba, D. J. Batstone, X. Flores-Alsina, and S. Tait, “A generalised chemical precipitation modelling approach in wastewater treatment applied to calcite,” *Water Res.*, vol. 68, pp. 342–353, Jan. 2015.

[29] P. Aagaard and H. C. Helgeson, “Thermodynamic and kinetic constraints on reaction rates among minerals and aqueous solutions; I, Theoretical considerations,” *Am. J. Sci.*, vol. 282, no. 3, pp. 237–285, Mar. 1982.

[30] E. V. Musvoto, M. C. Wentzel, R. E. Loewenthal, and G. A. Ekama, “Integrated chemical–physical processes modelling—I. Development of a kinetic-based model for mixed weak acid/base systems,” *Water Res.*, vol. 34, no. 6, pp. 1857–1867, Apr. 2000.

[31] S. C. Galbraith, P. A. Schneider, and A. E. Flood, “Model-driven experimental evaluation of struvite nucleation, growth and aggregation kinetics,” *Water Res.*, vol. 56, pp. 122–132, Jun. 2014.

[32] S. C. Galbraith and P. A. Schneider, “Modelling and simulation of inorganic precipitation with nucleation, crystal growth and aggregation: A new approach to an old method,” *Chem. Eng. J.*, vol. 240, pp. 124–132, Mar. 2014.

[33] V. W. Truesdale and J. Greenwood, “Latent disciplinal clashes concerning the batch dissolution of minerals, and their wider implications,” *Environ. Chem.*, vol. 15, no. 2, pp. 113–120, May 2018.

[34] K. S. L. Corre, E. Valsami-Jones, P. Hobbs, and S. A. Parsons, “Phosphorus Recovery from Wastewater by Struvite Crystallization: A Review,” *Crit. Rev. Environ. Sci. Technol.*, vol. 39, no. 6, pp. 433–477, Jun. 2009.

[35] E. Desmidt *et al.*, “Global Phosphorus Scarcity and Full-Scale P-Recovery Techniques: A Review,” *Crit. Rev. Environ. Sci. Technol.*, vol. 45, no. 4, pp. 336–384, Feb. 2015.

[36] Z. Yuan, S. Pratt, and D. J. Batstone, “Phosphorus recovery from wastewater through

microbial processes," *Curr. Opin. Biotechnol.*, vol. 23, no. 6, pp. 878–883, Dec. 2012.

[37] S. K. Ramasahayam, L. Guzman, G. Gunawan, and T. Viswanathan, "A Comprehensive Review of Phosphorus Removal Technologies and Processes," *J. Macromol. Sci. Part A*, vol. 51, no. 6, pp. 538–545, Jun. 2014.

[38] S. A. El-Shafai, F. A. El-Gohary, F. A. Nasr, N. Peter van der Steen, and H. J. Gijzen, "Nutrient recovery from domestic wastewater using a UASB-duckweed ponds system," *Bioresour. Technol.*, vol. 98, no. 4, pp. 798–807, Mar. 2007.

[39] E. Posadas, P.-A. García-Encina, A. Soltau, A. Domínguez, I. Díaz, and R. Muñoz, "Carbon and nutrient removal from centrates and domestic wastewater using algal–bacterial biofilm bioreactors," *Bioresour. Technol.*, vol. 139, pp. 50–58, Jul. 2013.

[40] N. Kishida, S. Tsuneda, J. H. Kim, and R. Sudo, "Simultaneous nitrogen and phosphorus removal from high-strength industrial wastewater using aerobic granular sludge," *J. Environ. Eng.*, vol. 135, no. 3, pp. 153–158, 2009.

[41] P. O. Bickers, R. Bhamidimarri, J. Shepherd, and J. Russell, "Biological phosphorus removal from a phosphorus-rich dairy processing wastewater," *Water Sci. Technol.*, vol. 48, no. 8, pp. 43–51, Nov. 2003.

[42] P. Wilfert, P. S. Kumar, L. Korving, G.-J. Witkamp, and M. C. M. van Loosdrecht, "The Relevance of Phosphorus and Iron Chemistry to the Recovery of Phosphorus from Wastewater: A Review," *Environ. Sci. Technol.*, vol. 49, no. 16, pp. 9400–9414, Aug. 2015.

[43] M. Valve, P. Rantanen, and J. Kallio, "Enhancing biological phosphorus removal from municipal wastewater with partial simultaneous precipitation," *Water Sci. Technol.*, vol. 46, no. 4–5, pp. 249–255, Aug. 2002.

[44] T. Clark, T. Stephenson, and P. A. Pearce, "Phosphorus removal by chemical precipitation in a biological aerated filter," *Water Res.*, vol. 31, no. 10, pp. 2557–2563, Oct. 1997.

[45] G. Crawford, G. Daigger, J. Fisher, S. Blair, and R. Lewis, *Enhanced Biological Phosphorus Removal Performance of the Traverse City MBR*, vol. 2007. Water Environment Federation, 2007.

[46] J. Barnard, S. Murthy, and C. deBarbadillo, *Development of Sustainable Approaches to Achieving Low Phosphorus Effluents*, vol. 2011. Water Environment Federation, 2011.

[47] L. Cubbage *et al.*, *A Green Alternative for Dissolved Nutrient Recovery in Wastewater Sidestreams*, vol. 2011. Water Environment Federation, 2011.

[48] N. Cullen, R. Baur, and P. Schauer, "Three years of operation of North America's first nutrient recovery facility," *Water Sci. Technol.*, vol. 68, no. 4, pp. 763–768, Aug. 2013.

[49] S. Hardy *et al.*, *Nutrient Recovery at the F. Wayne Hill Water Resources Center: Wasstrip Design and Full Scale Start Up*, vol. 2016. Water Environment Federation, 2016.

[50] A. Grooms, S. Reusser, A. Dose, A. Britton, and R. Prasad, *Operating Experience with Ostara Struvite Harvesting Process*, vol. 2015. Water Environment Federation, 2015.

[51] P. Schauer, R. Baur, J. Barnard, and A. Britton, *Increasing Revenue While Reducing Nuisance Struvite Precipitation: Pilot Scale Testing of the WASSTRIP Process*, vol. 2011. Water Environment Federation, 2011.

[52] M. Fabiyi, A. Britton, P. Schauer, A. Shaw, and R. Goel, *Applying process modeling with GPS-X^{TM} for Understanding the impact of the WASSTRIP^{TM} process on nutrient recovery systems*, vol. 2016. Water Environment Federation, 2016.

[53] M. Fabiyi, A. Menniti, P. Schauer, A. Britton, and R. Goel, *Modeling & Operational Case Study of a Full Scale Phosphorus Recovery System Coupled with WASSTRIP®: Factors to*

Consider in Model Development & Insights for Optimal P Recovery, vol. 2016. Water Environment Federation, 2016.

[54] "AirPrex® – CNP – Technology Water and Biosolids US." .

[55] J. Barnard, H. Phillips, and M. Steichen, *State-of-the-art recovery of phosphorus from wastewater*, vol. 2012. Water Environment Federation, 2012.

[56] B. Wisdom, B. V. Anderson, I. Avila, T. Gottschalk, K. Carson, and L. Cavanaugh, *Pilot-scale Evaluation of AirPrex® for Digestate Treatment*, vol. 2017. Water Environment Federation, 2017.

[57] M. S. Massey, J. G. Davis, J. A. Ippolito, and R. E. Sheffield, "Effectiveness of Recovered Magnesium Phosphates as Fertilizers in Neutral and Slightly Alkaline Soils," *Agron. J.*, vol. 101, no. 2, pp. 323–329, Mar. 2009.

[58] E. V. Musvoto, M. C. Wentzel, and G. A. Ekama, "Integrated chemical–physical processes modelling—II. simulating aeration treatment of anaerobic digester supernatants," *Water Res.*, vol. 34, no. 6, pp. 1868–1880, Apr. 2000.

[59] D. Mamais, P. A. Pitt, Y. W. Cheng, J. Loiacono, and D. Jenkins, "Determination of ferric chloride dose to control struvite precipitation in anaerobic sludge digesters," *Water Environ. Res.*, vol. 66, no. 7, pp. 912–918, Nov. 1994.

[60] D. Kim, B. Lee, S. Thomopoulos, and Y.-S. Jun, "In Situ Evaluation of Calcium Phosphate Nucleation Kinetics and Pathways during Intra- and Extrafibrillar Mineralization of Collagen Matrices," *Cryst. Growth Des.*, vol. 16, no. 9, pp. 5359–5366, Sep. 2016.

[61] N. Eliaz and N. Metoki, "Calcium Phosphate Bioceramics: A Review of Their History, Structure, Properties, Coating Technologies and Biomedical Applications," *Materials*, vol. 10, no. 4, p. 334, Mar. 2017.

[62] L.-W. Du *et al.*, "Structure of Clusters and Formation of Amorphous Calcium Phosphate and Hydroxyapatite: From the Perspective of Coordination Chemistry," *Cryst. Growth Des.*, vol. 13, no. 7, pp. 3103–3109, Jul. 2013.

[63] W. J. E. M. Habraken *et al.*, "Ion-association complexes unite classical and non-classical theories for the biomimetic nucleation of calcium phosphate," *Nat. Commun.*, vol. 4, p. 1507, 2013.

[64] A. S. Posner and F. Betts, "Synthetic amorphous calcium phosphate and its relation to bone mineral structure," *Acc. Chem. Res.*, vol. 8, no. 8, pp. 273–281, 1975.

[65] T. Clark, T. Stephenson, and P. A. Pearce, "Phosphorus removal by chemical precipitation in a biological aerated filter," *Water Res.*, vol. 31, no. 10, pp. 2557–2563, Oct. 1997.

[66] E. Paul, M. L. Laval, and M. Sperandio, "Excess Sludge Production and Costs Due to Phosphorus Removal," *Environ. Technol.*, vol. 22, no. 11, pp. 1363–1371, Nov. 2001.

[67] H. Hauduc *et al.*, "A dynamic physicochemical model for chemical phosphorus removal," *Water Res.*, vol. 73, no. Supplement C, pp. 157–170, Apr. 2015.

[68] C. Luedecke, S. W. Hermanowicz, and D. Jenkins, "Precipitation of Ferric Phosphate in Activated Sludge: A Chemical Model and Its Verification," *Water Sci. Technol.*, vol. 21, no. 4–5, pp. 325–337, Apr. 1989.

[69] S. Smith, I. Takács, S. Murthy, G. T. Daigger, and A. Szabó, "Phosphate Complexation Model and Its Implications for Chemical Phosphorus Removal," *Water Environ. Res.*, vol. 80, no. 5, pp. 428–438, May 2008.

[70] K. Fytianos, E. Voudrias, and N. Raikos, "Modelling of phosphorus removal from aqueous and wastewater samples using ferric iron," *Environ. Pollut.*, vol. 101, no. 1, pp. 123–

130, Jan. 1998.
[71] Y. Xu, Z. Chen, W. Ding, and J. Fan, “Responses of manure decomposition to nitrogen addition: Role of chemical composition,” *Sci. Total Environ.*, vol. 587–588, no. Supplement C, pp. 11–21, Jun. 2017.
[72] A. Atalay and B. Whitehead, “Thermodynamic Principles of Dittmarite Precipitation.”
[73] J. C. Heughebaert and G. H. Nancollas, “Solubility of octacalcium phosphate at 25 and 45.degree.C in the system calcium hydroxide-phosphoric acid-potassium nitrate-water,” *J. Chem. Eng. Data*, vol. 30, no. 3, pp. 279–281, Jul. 1985.
[74] V. Uskoković and D. Uskoković, “Nanosized Hydroxyapatite and Other Calcium Phosphates: Chemistry of Formation and Application as Drug and Gene Delivery Agents,” *J Biomed Mater Res*, no. 96B, pp. 152–191, 2011.
[75] H. Schoen, C. Grove, and J. Palmero, “The early history of crystallization,” *J. Chem. Educ.*, vol. 33, no. 8, p. 373, 1956.
[76] N. Variankaval, A. Cote, and M. Doherty, “From form to function: Crystallization of active pharmaceutical ingredients,” *AIChE J.*, vol. 54, no. 7, pp. 1682–1688.
[77] R. Hartel and S. Arun, “Sugar crystallization in food products,” *Crit. Rev. Food Sci. Nutr.*, vol. 30, no. 1, pp. 49–112, 1991.
[78] D. Kirwan and C. Orella, “Crystallization in the pharmaceutical and bioprocessing industries,” in *Handbook of Industrial Crystallization*, 2nd ed., 2002.
[79] A. Randolph and M. Larson, “MODELING CONTINUOUS AND BATCH CRYSTALLIZERS,” in *Theory of Particulate Processes*, 2nd ed., 1988, pp. 80–108.
[80] A. Randolph and M. Larson, “THE POPULATION BALANCE,” in *Theory of Particulate Processes*, 2nd ed., 1988, pp. 50–79.
[81] M. J. Hounslow, R. L. Ryall, and V. R. Marshall, “A discretized population balance for nucleation, growth, and aggregation,” *AIChE J.*, vol. 34, no. 11, pp. 1821–1832, 1988.
[82] M. Hanhoun, L. Montastruc, C. Azzaro-Pantel, B. Biscans, M. Frèche, and L. Pibouleau, “Simultaneous determination of nucleation and crystal growth kinetics of struvite using a thermodynamic modeling approach,” *Chem. Eng. J.*, vol. 215–216, pp. 903–912, Jan. 2013.
[83] C. Kazadi Mbamba, X. Flores-Alsina, D. John Batstone, and S. Tait, “Validation of a plant-wide phosphorus modelling approach with minerals precipitation in a full-scale WWTP,” *Water Res.*, vol. 100, pp. 169–183, Sep. 2016.
[84] I. Lizarralde *et al.*, “A new general methodology for incorporating physico-chemical transformations into multi-phase wastewater treatment process models,” *Water Res.*, vol. 74, pp. 239–256, May 2015.
[85] P. G. Koutsoukos and G. H. Nancollas, “The morphology of hydroxyapatite crystals grown in aqueous solution at 37°C,” *J. Cryst. Growth*, vol. 55, no. 2, pp. 369–375, Nov. 1981.
[86] E. V. Musvoto, M. C. Wentzel, and G. A. Ekama, “Integrated chemical–physical processes modelling—II. simulating aeration treatment of anaerobic digester supernatants,” *Water Res.*, vol. 34, no. 6, pp. 1868–1880, Apr. 2000.
[87] V. Snoeyink and D. Jenkins, *Water Chemistry*. John Wiley & Sons, 1980.
[88] P. L. Brezonik and W. Arnold, *Water chemistry*. New York: Oxford University Press, 2011.
[89] A. J. Giuffre, L. M. Hamm, N. Han, J. J. D. Yoreo, and P. M. Dove, “Polysaccharide chemistry regulates kinetics of calcite nucleation through competition of interfacial energies,” *Proc. Natl. Acad. Sci.*, vol. 110, no. 23, pp. 9261–9266, Jun. 2013.
[90] L. M. Hamm *et al.*, “Reconciling disparate views of template-directed nucleation through

measurement of calcite nucleation kinetics and binding energies," *Proc. Natl. Acad. Sci.*, vol. 111, no. 4, pp. 1304–1309, Jan. 2014.

[91] D. Gebauer, A. Völkel, and H. Cölfen, "Stable prenucleation calcium carbonate clusters," *Science*, vol. 322, no. 5909, pp. 1819–1822, 2008.

[92] A. Dey *et al.*, "The role of prenucleation clusters in surface-induced calcium phosphate crystallization," *Nat. Mater.*, vol. 9, no. 12, p. 1010, 2010.

[93] J. F. Lutsko and G. Nicolis, "Theoretical Evidence for a Dense Fluid Precursor to Crystallization," *Phys. Rev. Lett.*, vol. 96, no. 4, p. 046102, Feb. 2006.

[94] D. Erdemir, A. Y. Lee, and A. S. Myerson, "Nucleation of Crystals from Solution: Classical and Two-Step Models," *Acc. Chem. Res.*, vol. 42, no. 5, pp. 621–629, May 2009.

[95] A. Gavezzotti, "Molecular Aggregation of Acetic Acid in a Carbon Tetrachloride Solution: A Molecular Dynamics Study with a View to Crystal Nucleation," *Chem. – Eur. J.*, vol. 5, no. 2, pp. 567–576, Feb. 1999.

[96] M. Elimelech, J. Gregory, X. Jia, and R. A. Williams, "Chapter 1 - Introduction," in *Particle Deposition & Aggregation*, Woburn: Butterworth-Heinemann, 1995, pp. 3–8.

[97] G. Mie, "Zur kinetischen Theorie der einatomigen Körper," *Ann. Phys.*, vol. 316, no. 8, pp. 657–697.

[98] J. E. Jones and D. Sc, "On the determination of molecular fields. —II. From the equation of state of a gas," *Proc R Soc Lond A*, vol. 106, no. 738, pp. 463–477, Oct. 1924.

[99] J. N. Israelachvili, "7 - Repulsive Steric Forces, Total Intermolecular Pair Potentials, and Liquid Structure," in *Intermolecular and Surface Forces (Third Edition)*, San Diego: Academic Press, 2011, pp. 133–149.

[100] M. Elimelech, J. Gregory, X. Jia, and R. A. Williams, "Chapter 2 - Electrical properties of interfaces," in *Particle Deposition & Aggregation*, Woburn: Butterworth-Heinemann, 1995, pp. 9–32.

[101] M. M. Clark, *Transport Modelling for Environmental Engineers and Scientists*, 2nd ed. John Wiley & Sons, 2009.

[102] M. Elimelech, J. Gregory, X. Jia, and R. A. Williams, "Chapter 3 - Surface interaction potentials," in *Particle Deposition & Aggregation*, Woburn: Butterworth-Heinemann, 1995, pp. 33–67.

[103] P. Hiemenz, *Principles of Colloid and Surface Chemistry, Third Edition, Revised and Expanded, 3rd Edition /*, 3rd edition. CRC Press, 2016.

[104] M. Elimelech, J. Gregory, X. Jia, and R. A. Williams, "Chapter 6 - Modelling of aggregation processes," in *Particle Deposition & Aggregation*, Woburn: Butterworth-Heinemann, 1995, pp. 157–202.

[105] M. v. Smoluchowski, "Versuch einer mathematischen Theorie der Koagulationskinetik kolloider Lösungen," *Z. Für Phys. Chem.*, vol. 92U, no. 1, pp. 129–168, 1918.

[106] V. W. Truesdale and J. Greenwood, "Latent disciplinal clashes concerning the batch dissolution of minerals, and their wider implications," *Environ. Chem.*, vol. 15, no. 2, p. 113, 2018.

[107] E. L. Sjöberg, "A fundamental equation for calcite dissolution kinetics," *Geochim. Cosmochim. Acta*, vol. 40, no. 4, pp. 441–447, Apr. 1976.

[108] J. W. Tester, W. G. Worley, B. A. Robinson, C. O. Grigsby, and J. L. Feerer, "Correlating quartz dissolution kinetics in pure water from 25 to 625°C," *Geochim. Cosmochim. Acta*, vol. 58, no. 11, pp. 2407–2420, Jun. 1994.

[109] P. M. Dove and D. A. Crerar, "Kinetics of quartz dissolution in electrolyte solutions

using a hydrothermal mixed flow reactor," *Geochim. Cosmochim. Acta*, vol. 54, no. 4, pp. 955–969, Apr. 1990.

[110] O. S. Pokrovsky and J. Schott, "Kinetics and Mechanism of Dolomite Dissolution in Neutral to Alkaline Solutions Revisited," *Am. J. Sci.*, vol. 301, no. 7, pp. 597–626, Sep. 2001.

[111] R. Tang, G. H. Nancollas, and C. A. Orme, "Mechanism of Dissolution of Sparingly Soluble Electrolytes," *J. Am. Chem. Soc.*, vol. 123, no. 23, pp. 5437–5443, Jun. 2001.

[112] W. Wu and G. H. Nancollas, "The dissolution and growth of sparingly soluble inorganic salts: A kinetics and surface energy approach," *Pure Appl. Chem.*, vol. 70, no. 10, pp. 1867–1872, Oct. 1998.

[113] V. W. Truesdale, "Evidence and Potential Implications of Exponential Tails to Concentration Versus Time Plots for the Batch Dissolution of Calcite," *Aquat. Geochem.*, vol. 21, no. 5, pp. 365–396, Sep. 2015.

[114] A. Kamatani, J. P. Riley, and G. Skirrow, "The dissolution of opaline silica of diatom tests in sea water," *J. Oceanogr. Soc. Jpn.*, vol. 36, no. 4, pp. 201–208, Oct. 1980.

[115] V. W. Truesdale, "Silica Gel as a Surrogate for Biogenic Silica in Batch Dissolution Experiments at pH 9.2: Further Testing of the Shrinking Object Model and a Novel Approach to the Dissolution of a Population of Particles," *Aquat. Geochem.*, vol. 16, no. 1, pp. 101–126, Jan. 2010.

[116] V. W. Truesdale, "Sucrose Dissolution Studies Leading to a Generic Shrinking Object Model for Batch Dissolution of Regular-Shaped Particles," *Aquat. Geochem.*, vol. 15, no. 3, pp. 421–442, Aug. 2009.

[117] V. W. Truesdale, "Batch Dissolution Kinetics: The Shrinking Sphere Model with Salts and Its Potential Application to Biogenic Silica," *Aquat. Geochem.*, vol. 13, no. 4, pp. 267–287, Dec. 2007.

[118] K. S. Le Corre, E. Valsami-Jones, P. Hobbs, B. Jefferson, and S. A. Parsons, "Agglomeration of struvite crystals," *Water Res.*, vol. 41, no. 2, pp. 419–425, Jan. 2007.

[119] P. Larkin, "Chapter 6 - IR and Raman Spectra-Structure Correlations: Characteristic Group Frequencies," in *Infrared and Raman Spectroscopy*, P. Larkin, Ed. Oxford: Elsevier, 2011, pp. 73–115.

[120] F. Abbona and R. Boistelle, "Growth morphology and crystal habit of struvite crystals (MgNH4PO4 · 6 H2O)," *J. Cryst. Growth*, vol. 46, no. 3, pp. 339–354, Mar. 1979.

[121] A. K. Sarkar, "Hydration/dehydration characteristics of struvite and dittmarite pertaining to magnesium ammonium phosphate cement systems," *J. Mater. Sci.*, vol. 26, no. 9, pp. 2514–2518, 1991.

APPENDIX A: SUPPLEMENTARY FIGURES AND TABLES

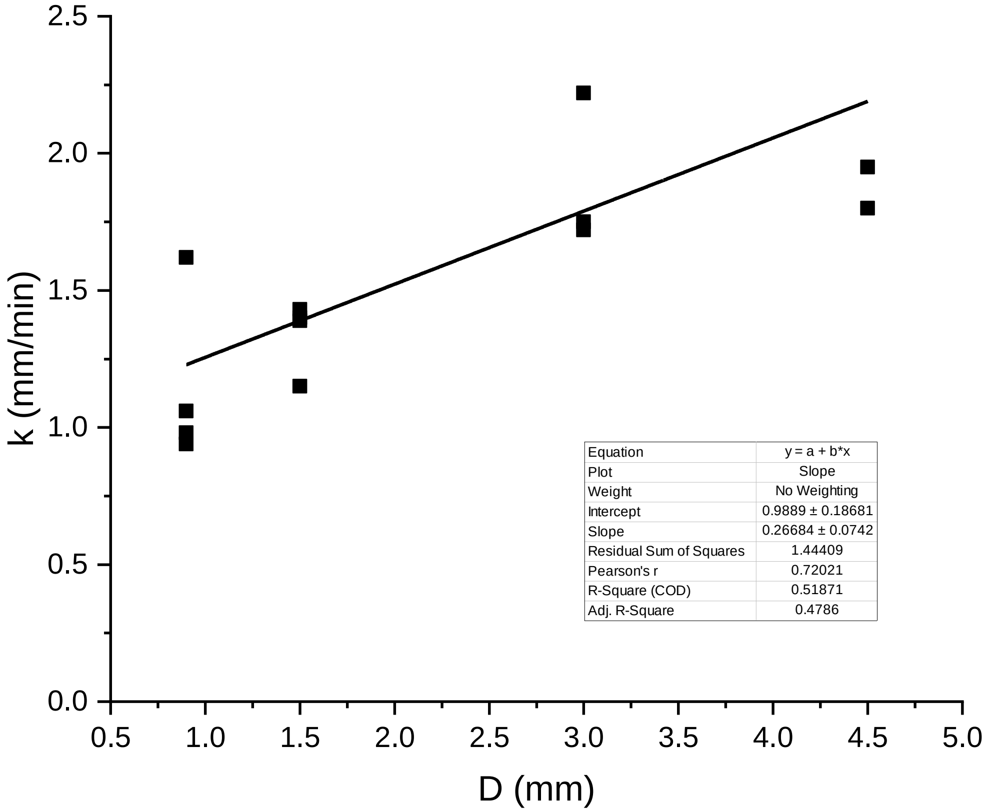

Figure 11. A weak correlation with size was found in the individual dissolution rate constants determined from the linearized SO model fit shown in figure 6.

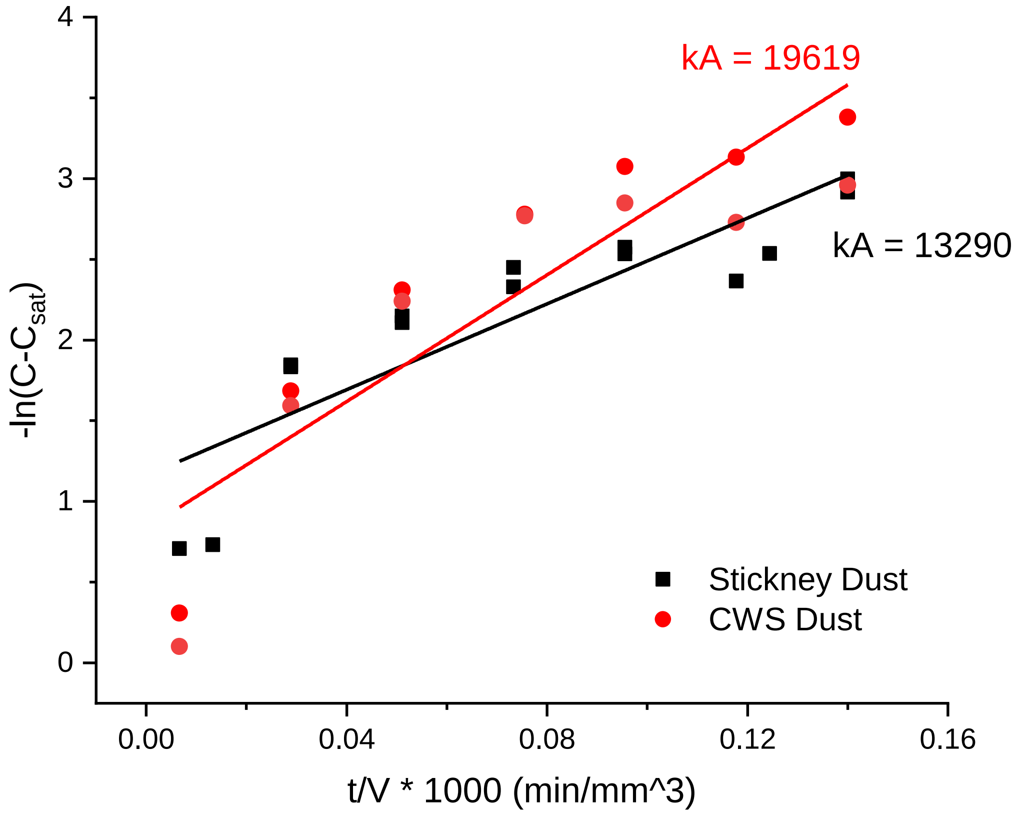

Figure 12. Time-series dissolution data fit to the linearized shrinking object model with a lumped dissolution rate constant (kA (mm^3/min)).

Table 4. Equilibrium P from IC

		Temperature (°C)					
		4.4		21.5		29.5	
Source	**Size**	**Average (mM P)**	**SD (mM P)**	**Average (mM P)**	**SD (mM P)**	**Average (mM P)**	**SD (mM P)**
CWS	450	2.90	0.08	5.21	0.10	6.88	0.33
	300	2.72	0.04	5.43	0.03	8.00	0.02
	150	2.63	0.01	5.52	0.02	8.10	0.06
	90	2.64	0.01	5.38	0.01	8.41	0.07
	35	3.79	0.00	6.87	0.07	7.96	0.11
	Dust	--	--	4.41	0.12	--	--
Stickney	300	--	--	1.97	0.05	--	--
	150	--	--	1.90	0.11	--	--
	90	--	--	2.44	0.12	--	--
	Dust	--	--	6.27	0.13	--	--
MWRD	12.5	--	--	2.44	0.07	--	--

Table 5. Equilibrium Solution Chemistry from ICP

		P		Mg		Fe		Ca		K	
Source	**Size**	**Average (mM P)**	**SD (mM P)**	**Average (mM Mg)**	**SD (mM Mg)**	**Average (mM Fe)**	**SD (mM Fe)**	**Average (mM Ca)**	**SD (mM Ca)**	**Average (mM K)**	**SD (mM K)**
CWS	450	6.684	0.407	6.328	0.574	0.008	0.001	0.091	0.012	0.027	0.002
	300	6.964	0.256	6.642	0.123	0.025	0.001	0.099	0.000	0.023	0.001
	150	6.650	0.101	6.639	0.141	0.015	0.001	0.078	0.005	0.020	0.001
	90	7.183	0.170	6.738	0.176	0.020	0.000	0.088	0.002	0.020	0.001
	35	7.585	0.231	6.767	0.071	0.004	0.000	0.118	0.012	0.063	0.005
	Dust	4.267	0.608	3.901	0.340	0.002	0.000	0.064	0.009	0.028	0.005
Stickney	300	1.832	0.159	1.636	0.088	0.000	0.000	0.093	0.014	0.026	0.003
	150	2.101	0.025	1.766	0.002	0.001	0.000	0.107	0.001	0.029	0.001
	90	2.828	0.045	2.430	0.023	0.002	0.000	0.115	0.004	0.033	0.001
	Dust	2.517	0.018	2.285	0.086	0.007	0.000	0.099	0.008	0.047	0.004
MWRD	12.5	7.603	0.285	6.767	0.096	0.006	0.000	0.201	0.012	0.054	0.007

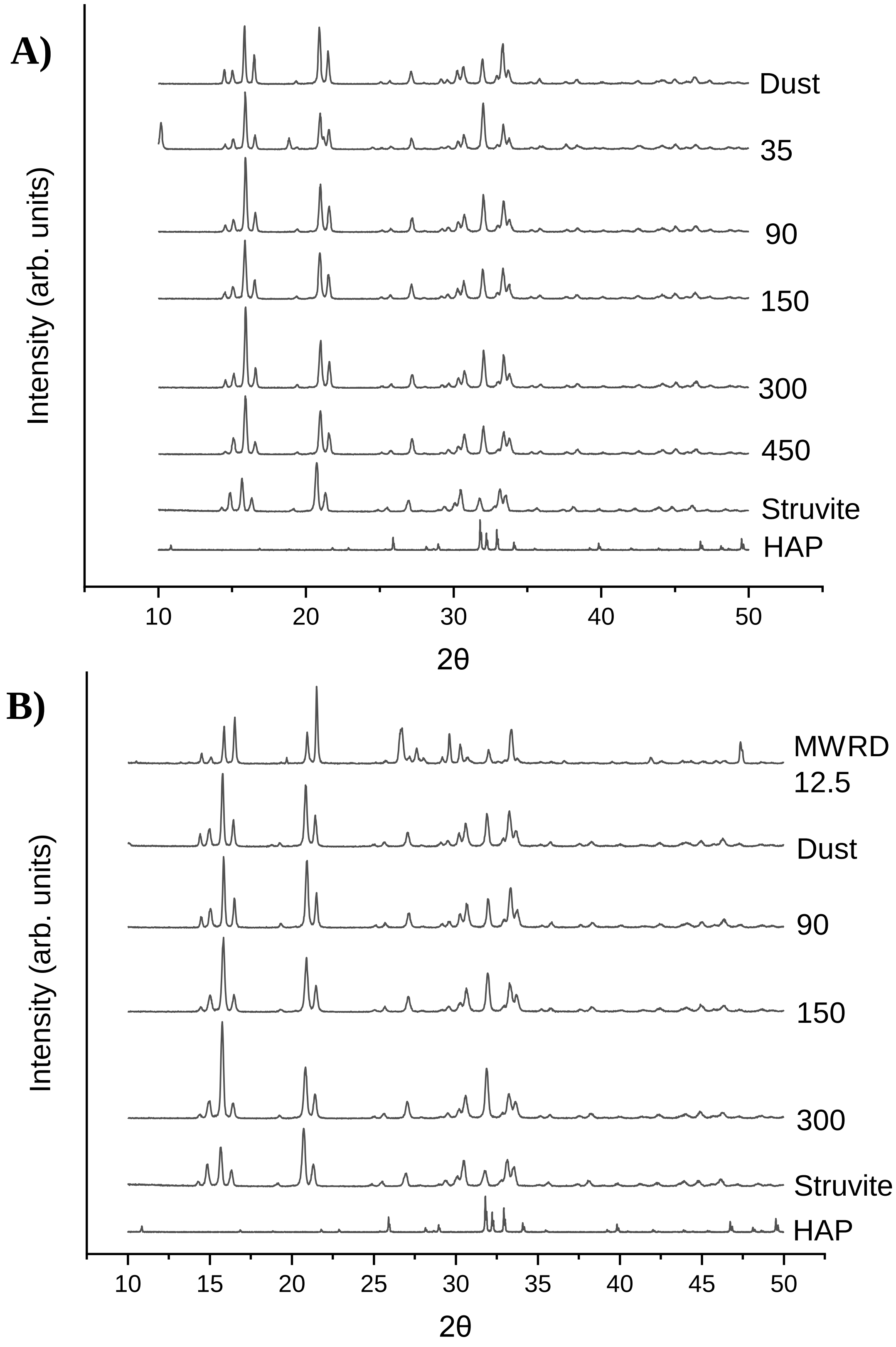

Figure 13. XRD spectra of all solids tested from A) CWS and B) Stickney and MWRD.

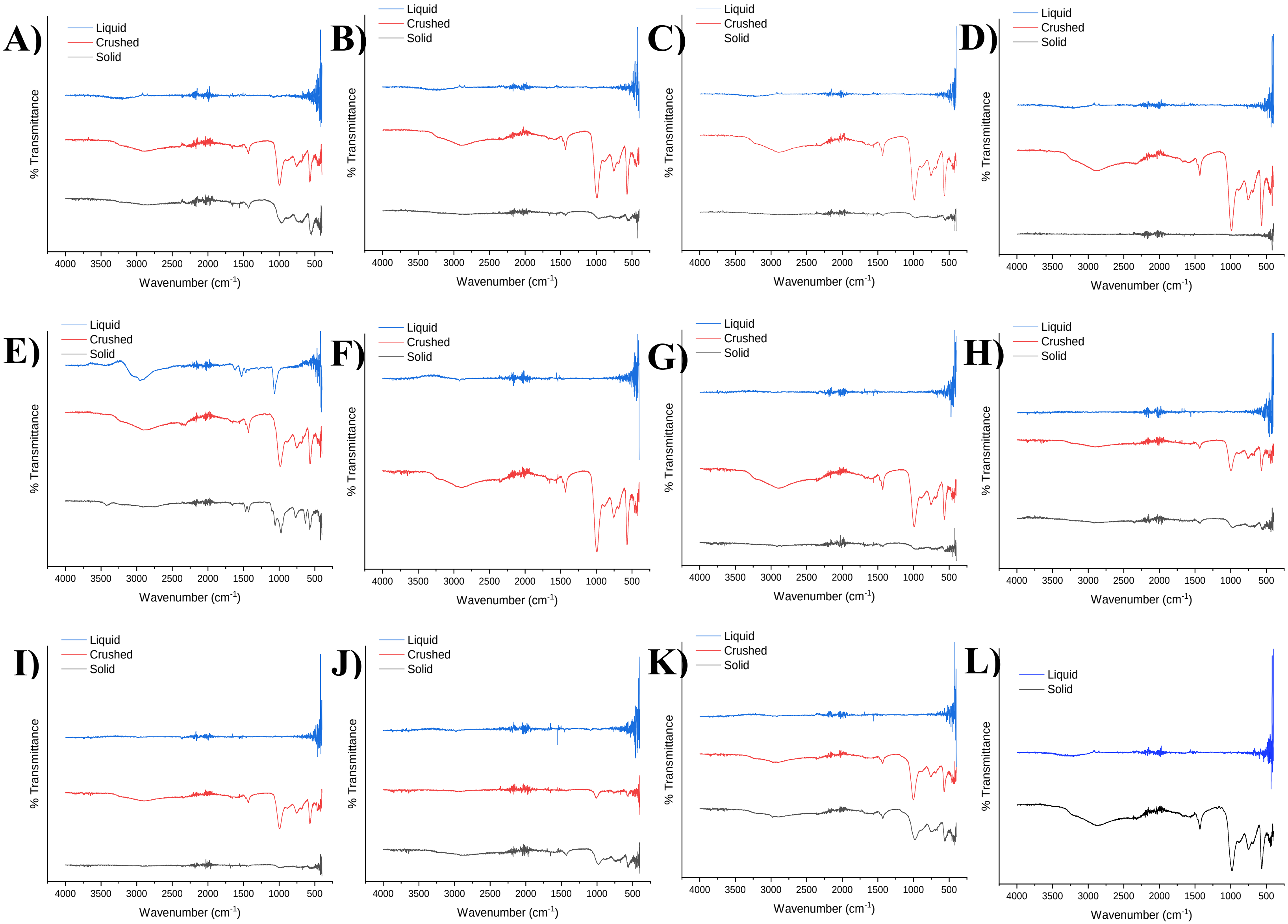

Figure 14. FTIR spectra of CWS A) SGN 450 – F) Dust, Stickney G) 300 – J) Dust, K) MWRD 12.5, and L) reference struvite.